Compositional variation of density and seismic velocities in natural peridotites at STP conditions: Implications for seismic imaging of compositional heterogeneities in the upper mantle

Cin-Ty Aeolus Lee

Department of Earth Science, Rice University, Houston, Texas, USA

[1]   Densities and elastic properties of solid natural spinel- and garnet-peridotite samples ($n = 133$) at standard temperature (T) and pressure (P) (STP) conditions were calculated for compositions ranging from Mg# ($100 \times$ Mg/(Mg + Fe)) of 86–94. The physical properties were used to investigate how natural compositional variations control density and seismic velocity. A corresponding set of compositional derivatives (d/dMg#) of density and seismic velocity is provided. Because the P and T derivatives of elastic moduli are very similar for different compositional end-members of peridotitic minerals, the variation of elastic moduli with Mg# at STP conditions holds at elevated P and T. Increased Mg# leads to a significant increase in V_S because of the sensitivity of mineral shear moduli to this parameter (dV_S/dMg# $= 0.0143 \pm 0.0009$ km s^{-1}). In contrast, the compressional wave velocity (V_P) is insensitive to Mg# and, instead, correlates weakly with increasing olivine abundance at STP conditions. The ratio V_P/V_S therefore exhibits a significant negative correlation with Mg# ($d(V_P/V_S)/d$Mg# $= -0.00407 \pm 0.00038$). Because the temperature dependency of V_P/V_S is small ($<\sim 0.04\%/100°$C) compared to the compositional dependency (1.7%/Mg# unit), the variation in V_P/V_S is a fairly robust measure of compositional variation even when temperature varies. Finally, a new density versus Mg# parameterization is derived. Combined with a compilation of bulk-rock Mg#s of peridotite xenoliths from cratonic lithospheric mantle, it is shown that the intrinsic density of cratonic mantle balances to within error its negative thermal buoyancy imposed by its cooler thermal state relative to upwelling asthenospheric mantle.   *INDEX TERMS:* 1025 Geochemistry: Composition of the mantle; 3909 Mineral Physics: Elasticity and anelasticity; 7207 Seismology: Core and mantle; 8120 Tectonophysics: Dynamics of lithosphere and mantle—general; *KEYWORDS:* xenolith, peridotite, seismic velocity, density, lithosphere, tectosphere

1. Introduction

[2] There has been a recent increase in the number of high-resolution seismic tomographic studies of the uppermost mantle with the intention of characterizing small variations in the thermal and compositional structure of the deep lithosphere. The ability to infer bulk composition variations in the uppermost mantle from seismic observations could have important implications for understanding mantle geodynamics and the petrogenesis of various upper mantle reservoirs. For example, not only is it important to delineate the physical differences between continental lithospheric mantle, oceanic lithospheric mantle, and asthenospheric mantle, much insight on the physics and chemistry of continent formation can be gained if subtle compositional variations within the continental lithospheric mantle can be seismically resolved. There is thus a growing need for assessing the degree to which seismic velocities vary as a function of temperature and composition in natural upper mantle samples.

[3] Here the effects of compositional variation on density and isotropic seismic velocities in upper mantle peridotites are investigated by directly studying a group of natural peridotites ($n = 133$), spanning the primary compositional range seen in nature (($100 \times$ Mg/(Mg + Fe) = Mg# $\sim 86-88$) to highly residual compositions (Mg# $\sim 93-94$)). As a first step toward inverting seismic velocity anomalies for compositional variations, compositional derivatives (d/dMg#) between calculated standard state (STP) seismic velocities and various bulk compositional indices are presented here. As will be discussed, the pressure and temperature derivatives of the compositional end-members of peridotitic minerals are very similar, and therefore the compositional derivatives of elastic moduli with respect to Mg# at STP conditions are applicable to elevated pressure and temperature. Seismic velocities are calculated using knowledge of mineral compositions, mineral modes, and experimentally

determined elastic moduli of mineral end-members. The rationalization for confining the velocity calculations to STP conditions rather than in situ pressures and temperatures is that the pressure and temperature derivatives of the elastic moduli for all mineral end-members are not known. However, the STP compositional derivatives of seismic velocities are not likely to depend significantly on pressure and temperature, and therefore the results presented here are applicable to interpreting relative variations in seismic velocity at upper mantle conditions.

[4] The approach here in determining seismic velocities of natural peridotites differs fundamentally from studies in which seismic velocities are calculated using theoretical mineral assemblages in the mantle as determined from thermodynamic considerations [*Jordan*, 1979; *Kelly et al.*, 2003]. In the latter approach, extrapolations of thermodynamic parameters to high pressure and temperature may cause systematic biases in calculated mineral modes. In addition, the thermodynamic approach often requires some simplification of the compositional space because the thermodynamic parameters in more complicated systems have not yet been fully worked out. Finally, the thermodynamic approach assumes that the mineral mode assemblage in the modeled system is in equilibrium (modal equilibrium), which may or may not be the case, depending on the prescribed lengthscale of the system. The approach of using natural peridotites is advantageous in that there is no a priori assumption of modal equilibrium and there is no need to rely on any thermodynamic assumptions or simplifications in calculating mineral modes. In addition, the use of natural peridotites allows for the assessment of the true natural variation in peridotite compositions in so far as the sampling of peridotites (as xenoliths or tectonically obducted massifs) is representative of the upper mantle. The drawback of using natural peridotite is the possibility of internal mineral heterogeneity (as opposed to modal disequilibrium) due to local disequilibrium. Such heterogeneity can give rise to a difficult-to-quantify error in the calculation of mineral modes and mineral elastic moduli.

[5] It is important to recognize that other lithologies occur in the upper mantle, e.g., eclogites, Fe-rich ultramafics (e.g., olivine cumulates and/or pyroxenites with Mg# < 86), and recycled sediment. Although these lithologies are of interest, they are significantly less abundant than peridotites with Mg#s > 86. As a first step toward understanding compositional variation in the mantle, this manuscript focuses solely on the abundant peridotite lithologies. The effects of a melt phase or dissolved hydrogen in silicate phases on elastic moduli are not discussed here. The effects of anelasticity (seismic attenuation) and anisotropy are not considered here.

2. Review of the Composition of Upper Mantle Peridotites and Minerals

[6] A number of detailed reviews on the compositional variations of upper mantle peridotites and their constituent minerals can be found in the literature [*Nixon et al.*, 1981; *Boyd*, 1987, 1989; *McDonough and Frey*, 1989; *Menzies*, 1989; *McDonough*, 1990; *Menzies et al.*, 1991; *McDonough and Sun*, 1995; *Griffin et al.*, 1999; *Poudjom et al.*, 2001]. However, a brief review summarizing the main composi-

tional features of peridotites and their minerals "in the context" of seismic velocity calculations is necessary. Seismic velocities of upper mantle peridotites have been estimated previously without accounting for all compositional effects. This review is intended to show the entire compositional variation in peridotite mineralogies so that more accurate densities and elastic moduli can be calculated.

2.1. Mineralogic and Major-Element Variations

[7] Peridotites are olivine-rich rocks containing variable amounts of orthopyroxene, clinopyroxene, and an aluminous phase (garnet or spinel). A number of accessory phases, such as phlogopite, amphibole, rutile, perovskite, ilmenite, sulfides, carbonates, melilite, and/or zircon can also be found in peridotites. However, since these accessory phases rarely amount to more than a few percent of the bulk rock, their contribution to seismic velocities and densities are ignored here.

[8] The presence of spinel or garnet in a peridotite depends primarily on pressure and bulk composition. For fertile peridotites (e.g., those that have experienced very little melt extraction), the spinel-garnet transition occurs at ~1.5 GPa (or ~45 km [*O'Neill*, 1981]). Using the fertile peridotite composition as a reference, the following metamorphic facies terminology is defined: peridotites derived from pressures <1.5 GPa are referred to as "spinel-facies peridotites" because spinel is the stable aluminous phase, while those derived from >1.5 GPa are referred to as "garnet-facies peridotites" because garnet is the stable aluminous phase. In refractory peridotites (e.g., those that have experienced significant melt extraction), the increased Cr content of residual spinels depresses the spinel-garnet transition so that the first appearance of garnet is suppressed to pressures as high as ~3 GPa (or ~90 km; [*O'Neill*, 1981; *Girnis and Brey*, 1999]), depending on the Cr/(Cr + Al) of the spinel. These refractory peridotites, which contain Cr-rich spinel instead of garnet, but are otherwise derived from pressures greater than 1.5 GPa, are referred to here as "garnet-facies spinel-peridotites" [cf. *Lee and Rudnick*, 1999].

[9] Figure 1a shows the observed range in peridotite mineralogy in olivine-orthopyroxene-clinopyroxene wt % space (excluding cumulates). Yellow squares represent spinel-peridotites collected from Phanerozoic continental lithospheric mantle and oceanic mantle. The compositional array represented by such peridotites is generally taken to reflect progressive extraction of partial melt [*Boyd*, 1989]. Figure 1b shows how Mg# and olivine mode of Phanerozoic peridotites varies as melt is progressively extracted (arrow). Primitive peridotites, i.e., those that have experienced minor amounts of melt extraction, are characterized by Mg#s of ~86–89 and significant amounts of clinopyroxene and orthopyroxene in addition to olivine; such peridotites are classified as lherzolites. With increasing degree of melting, clinopyroxene and orthopyroxene modes decrease and Mg# increases in the residual peridotite; peridotites with zero to <5 wt % clinopyroxene are classified as harzburgites. When enough melt has been extracted (e.g., >20 wt %) to exhaust not only clinopyroxene but also orthopyroxene (<10 wt %), an olivine-rich residue (dunite) is generated. Tables 1a and 1b shows additional compositional and mineralogic information for a small selection of natural spinel-peridotites and garnet-peridotites.
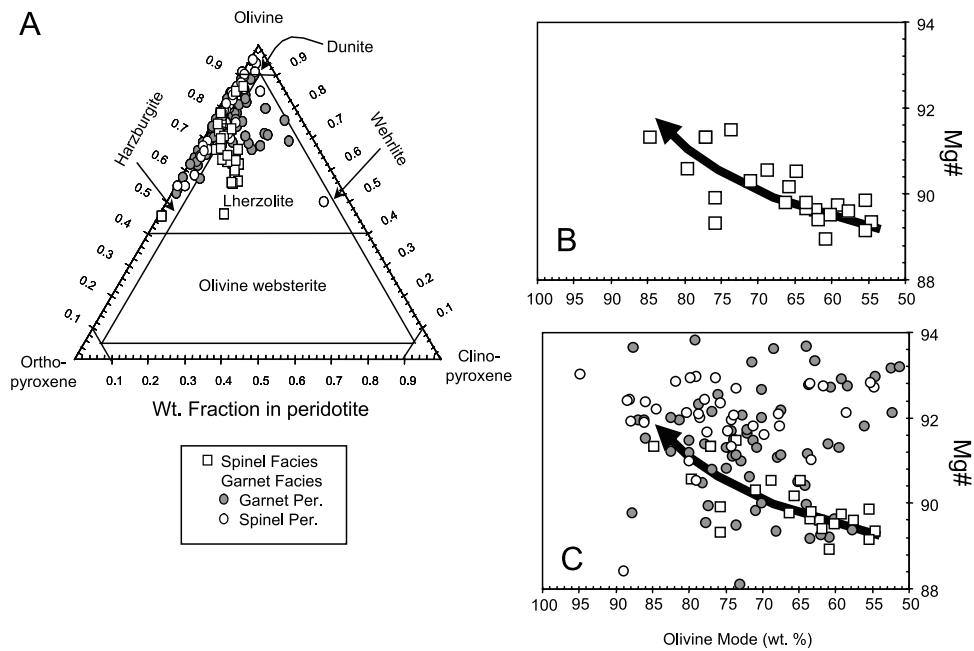
Figure 1. (a) Olivine-orthopyroxene-clinopyroxene ternary mode diagram expressed in terms of weight fraction. (b) Olivine mode versus bulk molar $100 \times Mg/(Mg + Fe) = Mg\#$ in spinel-facies spinel-peridotites; arrow shows the "approximate" trend displayed by peridotite residues with progressive melt extraction. (c) Identical to Figure 1b, but garnet-peridotites and garnet-facies spinel-peridotites have been superimposed. Garnet-facies peridotites, many of which are from cratonic localities, fall off the melting trend in Figure 1b (see text for discussion).

[10] In summary, progressive melt extraction results in an increase in Mg# and a decrease in orthopyroxene/olivine ratio [cf. *Boyd*, 1989]. However, in some instances, such as for some Archean peridotite xenoliths from the South African craton, there appears to be a number of peridotites that have excess orthopyroxene for a given Mg# [*Boyd*, 1989], i.e., they fall to the right of the melt-depletion arrow in Figure 1c. Although it is generally agreed that this excess orthopyroxene is a result of additional petrogenetic process/es superimposed on earlier melt extraction event/s [*Boyd*, 1989], the responsible petrogenetic process is still hotly debated [*Rudnick et al.*, 1994; *Kelemen et al.*, 1998; *Herzberg*, 1999]. This paper concerns only the determination of seismic velocities and densities of natural peridotites, so although the petrogenesis of these rocks is irrelevant for the purposes of this manuscript, all peridotite samples regardless of petrogenetic origin are fully incorporated into the database in order to describe the entire variation in upper mantle peridotite.

2.2. Variations in Mineral Composition

[11] Figures 2–4 show the range in compositions typically displayed in the major minerals in peridotites ranging from Mg# ∼ 86–94. Figures 2a and 2b show the compositional range displayed by clinopyroxenes and orthopyroxenes in terms of Mg, Fe, and Ca. Figures 3a and 3b show variations in the amount of Cr_2O_3 and Al_2O_3 in pyroxenes; garnet-facies pyroxenes typically show lower Al contents because most of the Al in the bulk rock is partitioned into garnet. It will be shown later that Al has a small but significant effect on the elastic moduli of pyroxenes. Figures 2c and 3c show the compositional variation of garnets; peridotitic garnets are invariably pyrope-rich, with

small but variable amounts of grossular and almandine components. Figure 4 shows the compositional variation of spinels in spinel-facies and garnet-facies spinel-peridotites (see above for definition of garnet-facies spinel peridotite). Spinel-facies peridotites consist predominantly of aluminous spinels, whereas the spinels in garnet-facies spinel-peridotites are typically Cr-rich [cf. *Lee and Rudnick*, 1999].

3. Peridotite Data Set

[12] The peridotite database ($n = 133$) used here for calculating elastic moduli consists of data from the literature, in which bulk-rock and mineral composition data are both reported. The data set comprises obducted massif peridotites and mantle xenoliths erupted through continental lithosphere, representing Archean to Phanerozoic continental lithospheric mantle. Peridotites from Archean lithospheres include South African, Tanzanian, and Siberian cratonic peridotites [*Boyd*, 1987; *Boyd and Mertzman*, 1987; *Boyd et al.*, 1993; *Lee and Rudnick*, 1999]. Peridotites from Proterozoic regions include peridotites from southwestern USA (Colorado Plateau) and ultramafic massifs in western Europe [*Ehrenberg*, 1982; *Frey et al.*, 1985; *Wilshire et al.*, 1988, 1991]. Those from Phanerozoic regions include southwestern USA and North American Cordilleran xenolith suites [*Francis*, 1987; *Shi et al.*, 1998].

4. Methods
4.1. Mineral Proportions

[13] Mineral mass proportions were determined by inversion of bulk composition data (XRF) and mineral composition data (electron microprobe). The following oxides

Table 1a. Peridotite Examples: Natural Spinel-Peridotites and Natural Garnet-Peridotites

	OPX	CPX	GT	OL	Bulk
Spinel-Peridotite 1					
Mode wt%	**28.28**	**14.54**	**54.59**	**2.59**	
SiO$_2$	55.07	51.94	40.99	0.33	45.19
TiO$_2$	0.08	0.39	0.01	0.06	0.09
Al$_2$O$_3$	4.26	6.10	0.03	57.27	3.53
Cr$_2$O$_3$	0.31	0.61	0.01	9.40	
FeO	6.25	2.84	9.93	11.59	8.15
MnO	0.13	0.10	0.14	0.08	0.13
MgO	32.94	15.14	48.80	20.80	38.35
NiO	0.00	0.00	0.36	0.17	
CaO	0.63	20.66	0.05	0.00	3.18
Na$_2$O	0.08	1.56	0.00	0.00	0.27
Total	99.8	99.3	100.3	99.4	98.9
Mg#[a]	90.38	90.48	89.76	76.19	89.35
ρ, g cm^{-3}	3.298	3.318	3.357	3.857	3.348
K, Gpa	106.2	109.4	129.2	201.4	120.8
G, Gpa	73.4	63.7	78.0	104.6	75.1
V_P, km s^{-1}	7.87	7.65	8.34	9.40	8.12
V_S, km s^{-1}	55.07	51.94	40.99	0.33	45.19
Spinel-Peridotite 2					
Mode wt%	**22.88**	**1.29**	**73.61**	**2.22**	
SiO$_2$	56.10	53.32	40.98	0.09	43.97
TiO$_2$	0.00	0.04	0.01	0.06	0.02
Al$_2$O$_3$	2.55	3.17	0.03	26.14	1.31
Cr$_2$O$_3$	0.86	1.41	0.04	42.49	
FeO	5.16	2.69	8.32	14.62	7.54
MnO	0.14	0.07	0.12	0.21	0.12
MgO	33.37	17.83	50.08	16.58	45.43
NiO	0.00		0.42	0.21	
CaO	1.22	20.37	0.11	0.00	0.63
Na$_2$O	0.05	0.71	0.00	0.00	0.01
Total	99.5	99.6	100.1	100.4	99.0
Mg#[a]	92.02	92.20	91.48	66.91	91.48
ρ, g cm^{-3}	3.289	3.319	3.340	4.279	3.349
K, Gpa	106.4	109.7	129.2	199.3	124.5
G, Gpa	73.6	65.5	78.5	111.0	77.8
V_P, km s^{-1}	7.89	7.70	8.37	9.01	8.26
V_S, km s^{-1}	56.10	53.32	40.98	0.09	43.97
Garnet-Peridotite 1					
Mode wt%	**9.79**	**14.00**	**15.38**	**60.84**	
SiO$_2$	55.96	54.18	42.40	40.27	43.28
TiO$_2$	0.20	0.38	0.73	0.03	0.21
Al$_2$O$_3$	2.02	3.45	21.52	0.06	3.89
Cr$_2$O$_3$	0.30	0.65	2.06	0.05	0.77
FeO	5.78	4.35	7.05	9.60	8.34
MnO	0.11	0.12	0.25	0.09	0.15
MgO	32.94	20.35	21.57	49.47	38.67
NiO				0.36	
CaO	1.70	13.78	4.29	0.12	2.74
Na$_2$O	0.30	1.82			0.29
Total	99.3	99.1	100.2	100.1	98.1
Mg#[a]	91.04	89.29	84.51	90.18	89.21
ρ, g cm^{-3}	3.290	3.314	3.697	3.360	3.399
K, Gpa	106.5	108.2	171.1	129.2	129.2
G, Gpa	73.2	66.7	171.1	78.2	78.5
V_P, km s^{-1}	7.88	7.71	10.39	8.34	8.29
V_S, km s^{-1}	4.72	4.49	6.80	4.82	4.81
Garnet-Peridotite 2					
Mode wt%	**20.03**	**0.36**	**5.08**	**74.53**	
SiO$_2$	57.27	54.18	41.56	40.16	43.86
TiO$_2$	0.21	0.46	0.74	0.03	0.11
Al$_2$O$_3$	1.04	2.75	19.61	0.02	1.19
Cr$_2$O$_3$	0.34	1.34	4.07	0.04	
FeO	5.02	3.32	6.45	8.26	7.85
MnO	0.11	0.09	0.27	0.01	0.13
MgO	35.24	19.11	24.97	50.66	46.24
NiO	0.12	0.09	0.01	0.35	
CaO	1.05	15.57	4.70	0.06	0.53
Na$_2$O	0.36	2.30	0.11	0.00	0.08

Table 1a. (continued)

	OPX	CPX	GT	OL	Bulk
Total	100.8	99.2	102.5	99.6	100.0
Mg#[a]	92.60	91.12	87.35	91.62	91.31
ρ, g cm^{-3}	3.276	3.313	3.730	3.343	3.349
K, Gpa	106.4	108.4	170.5	129.2	126.0
G, Gpa	73.8	65.5	170.5	78.6	78.3
V_P, km s^{-1}	7.91	7.68	10.33	8.37	8.29
V_S, km s^{-1}	4.75	4.45	6.76	4.85	4.84
Garnet-Peridotite 3					
Mode wt%	**24.06**	**1.77**	**2.72**	**71.45**	
SiO$_2$	57.63	55.39	42.23	41.25	45.06
TiO$_2$	0.00	0.00	0.01		0.07
Al$_2$O$_3$	0.68	2.53	22.85		0.85
Cr$_2$O$_3$	0.20	1.75	1.78		
FeO	4.20	1.22	7.50	6.88	5.99
MnO	0.11	0.05	0.47	0.07	0.11
MgO	37.36	16.31	21.46	52.59	47.03
NiO	0.00	0.00	0.00	0.36	
CaO	0.18	21.84	4.52	0.02	0.56
Na$_2$O	0.03	2.00	0.01		0.08
Total	100.4	101.1	100.8	101.2	100.0
Mg#[a]	94.07	95.97	83.61	93.16	93.33
ρ, g cm^{-3}	3.258	3.287	3.704	3.322	3.317
K, Gpa	106.4	109.2	171.3	129.1	123.8
G, Gpa	74.5	62.4	171.3	79.1	78.0
V_P, km s^{-1}	7.94	7.65	10.39	8.40	8.29
V_S, km s^{-1}	4.78	4.36	6.80	4.88	4.85

[a]Mg# = 100 × Mg/(Mg + Fe).

were used for the inversion: CaO, MgO, FeO, Al$_2$O$_3$, and SiO$_2$. In these calculations, the composition of each mineral phase was assumed to be homogeneous. It is assumed that the peridotite sample consists of four phases: orthopyroxene, clinopyroxene, olivine, and an aluminous phase (either garnet or spinel but not both). Petrographic observations were relied upon to determine whether garnet or spinel was the aluminous phase (samples with coexisting garnet and spinel were omitted from the study). Mineral mass proportions, X_i, were determined by matrix inversion via $\mathbf{X} = (\mathbf{C}^T\mathbf{C})^{-1}\mathbf{C}^T\mathbf{B}$, $\mathbf{X}$ is the 4×1 column matrix consisting of mineral mass proportions (X_i), $\mathbf{C}$ is the 5×4 mineral composition matrix, $\mathbf{C}^T$ is the transpose of $\mathbf{C}$, and $\mathbf{B}$ is the 5×1 bulk composition column matrix.

[14] The main uncertainties in the inverse approach result from (1) the presence of heterogeneous mineral compositions and (2) the presence of accessory metasomatic phases, such as phlogopite, sulfides, ilmenite, rutile, carbonate, and/

Table 1b. Peridotite Examples: Primitive Mantle Models[a]

	M&S	T&M
SiO$_2$	45	49.9
TiO$_2$	0.201	0.16
Al$_2$O$_3$	4.45	3.65
Cr$_2$O$_3$	0.384	0.44
FeO	8.05	8
MnO	0.135	0.13
MgO	37.8	35.15
NiO	0.25	0.25
CaO	3.55	2.9
Na$_2$O	0.36	0.34
Total	100.2	100.9
Mg#	89.3	88.7

[a]Both models are taken from *McDonough and Sun* [1995]. M&S, McDonough and Sun; T&M, Taylor and McLennan.
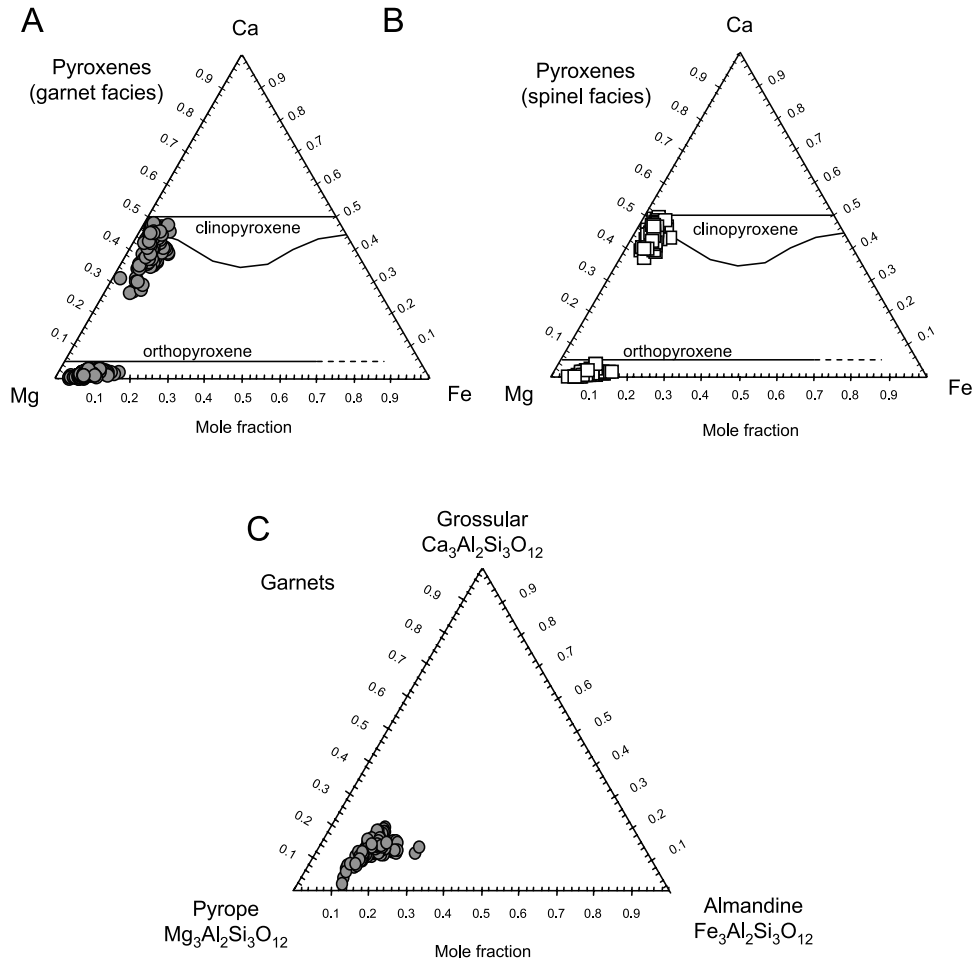
Figure 2. (a) Pyroxene ternary diagram in garnet-facies peridotites expressed in mole fraction of respective cation end-member in pyroxene. (b) Same as Figure 2a but for pyroxenes in spinel-facies peridotites. (c) Garnet ternary diagram expressed in mole fraction of respective cation end-member in garnet.

or quenched glasses. These accessory phases typically amount to less than 0.5–1% of the total mass of the rock, and even if present, could have been introduced during late-stage metasomatism or during entrainment in the host magma. Samples were initially omitted if there were large-scale metasomatic effects or heterogeneous mineral compositions described in the literature. Otherwise, samples with residuals (observed bulk composition versus calculated bulk composition) greater than 0.7% were omitted on the assumption that mineral heterogeneity or accessory metasomatic phases were present.

[15] This inverse approach is identical to that taken by *Boyd and McAllister* [1976]. However, Boyd and McAllister included Cr_2O_3 as an additional constraint. Cr_2O_3 data were not available for all samples in the compilation, so it was not used in the mode calculations. In the absence of a comprehensive mineral composition data set, mineral modes can be estimated by calculating the theoretical equilibrium mineral assemblage of a given bulk composition for fixed pressure and temperature using thermodynamic considerations. The first attempt to do such calculations made use of simple mass balance and empirical mass action relationships between the

major-element compositions of each mineral phase [*Jordan*, 1979]. Thermodynamic calculations should in theory yield the "equilibrium" mineral assemblage and mineral compositions if the thermodynamic model is accurate. In many cases, assumptions and simplifications must be used to extrapolate calculations to pressures, temperatures, and bulk compositions of interest. Some of the assumptions made by Jordan include constant equilibrium coefficients (e.g., independent of temperature and pressure) and simplified mineral compositions. Orthopyroxene was assumed to contain no Al_2O_3, but the Al_2O_3 content of orthopyroxenes in ultramafic xenoliths is not negligible as up to a few wt % Al_2O_3 can be present in orthopyroxene depending on temperature and pressure.

[16] The inverse approach taken here gives the most accurate picture of the true mineral assemblage in a peridotite sample as there are no assumptions other than the assumption of mineral homogeneity (see section 4.4). For the purposes of this study, it is assumed that the measured mineral assemblage of a peridotite xenolith or a massif peridotite reflects the state they last resided in the mantle, i.e., there has been no change in mineral assemblage/
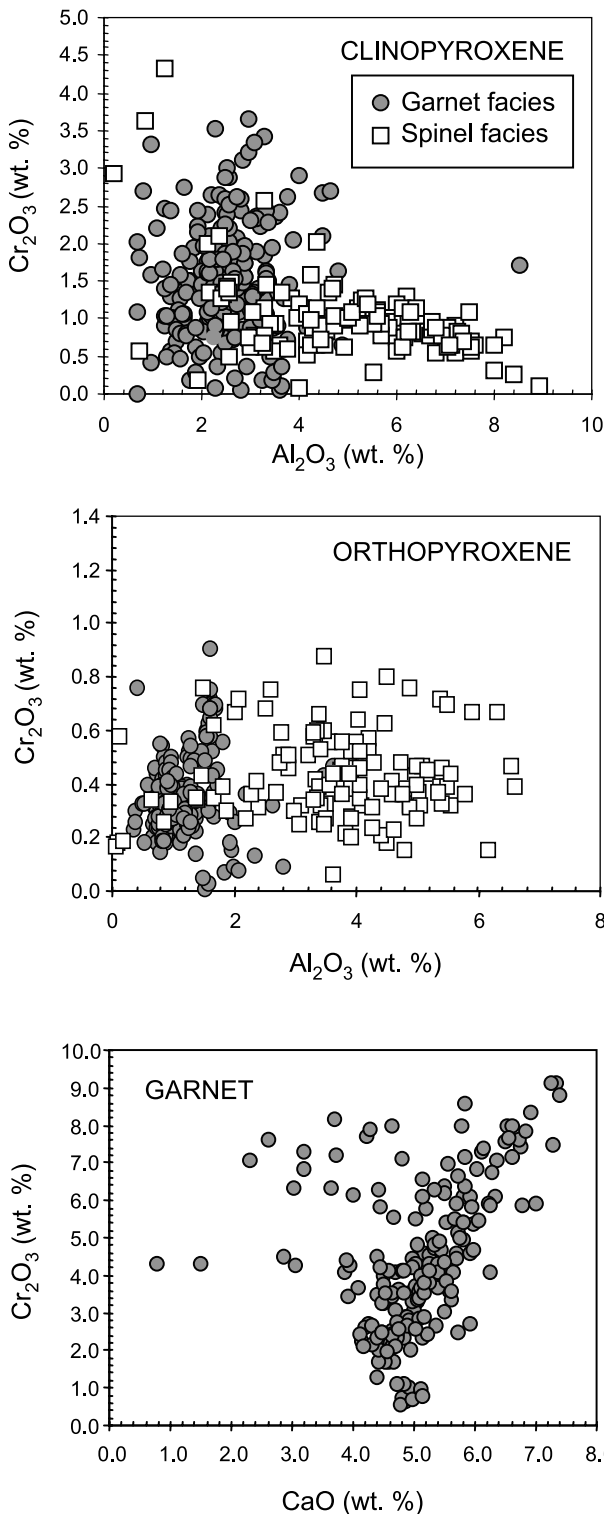
Figure 3. (a) Cr_2O_3 versus Al_2O_3 in clinopyroxenes (expressed in wt %). (b) Cr_2O_3 versus Al_2O_3 in orthopyroxenes. (c) Cr_2O_3 versus CaO in garnet.

composition during transport from mantle conditions to the surface of the Earth.

4.2. Density Calculations

[17] The following steps were followed for calculating bulk rock densities. Mineral densities were calculated using

mixing models to describe compositional solid solutions as a function of end-member molar volumes (cm^3 $mole^{-1}$). The mixing models for olivine, orthopyroxene, garnet, and spinel were taken exactly from the work of *Brey et al.* [1999] and that of clinopyroxene was constructed analogous to the model of Brey et al. For olivine and pyroxene, linear additivity of molar volumes was assumed. For spinel and garnet, nonideal mixing effects were accounted for as described below. Nonidealities included the effects of inter-site reciprocal reactions and intrasite interactions. Mineral densities were then calculated by dividing the formula weight of the mineral by its molar volume. The density of the bulk rock was then calculated by linear additivity of the densities according to the mass fraction of each mineral. The mass fraction instead of the volume fraction was used because mass fractions are more efficiently determined than volume fractions; the former can be determined by inversion of bulk compositional and mineral data, whereas the latter requires tedious point-counting techniques. The errors introduced by using mass fraction instead of volume fraction are negligible. Molar volumes of mineral end-member components are given in Table 2 (nonideal mixing terms are given in Table 3).

4.2.1. Olivine

[18] Olivine stoichiometry follows $(Mg,Fe)_2SiO_4$, hence it is described using the following components: forsterite (Mg_2SiO_4) and fayalite (Fe_2SiO_4). Mixing between the two end-members was assumed to be ideal, which yields $V_{Ol} = V_{Fo}X_{Mg} + V_{Fa}(1 - X_{Mg})$ where $X_{Mg} = Mg/(Mg + Fe)$, and Mg and Fe represent the atomic proportions on a 4-oxygen basis.

4.2.2. Spinel

[19] The chemistry of spinels in ultramafic rocks can be expressed as $(Mg,Fe)(Cr,Al)_2O_4$. The following end-member components are used to describe spinel: chromite ($FeCr_2O_4$), spinel ($MgAl_2O_4$), and picrochromite ($MgCr_2O_4$). It is assumed that Cr occurs only in the +3 valence state, so it occurs only in the tetrahedral site. The mixing model of *Brey et al.*
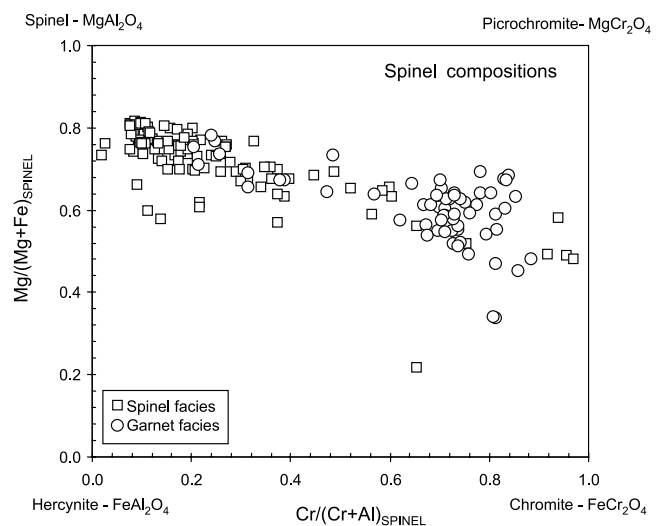

Figure 4. Molar $Mg/(Mg + Fe)$ versus molar $Cr/(Cr + Al)$ in spinels from spinel-facies and garnet-facies peridotites.

Table 2. Parameters

	Abbreviated Symbol	Molar Volume (V),[a] cm³ mole⁻¹	Bulk Modulus[b]			Shear Modulus[c]			Thermal Expansivity[d]		
			K_S, GPa	dK_S/dP	dK_S/dT, Gpa °K⁻¹	G, Gpa	DG/dP	dG/dT, Gpa K⁻¹	α_0, K⁻¹ × 10⁻⁵	α_1, K⁻² × 10⁻⁹	α_2, K
					Pyroxene						
$MgAlAlSiO_6$	Mg-Ts	60.4									
$MgCrAlSiO_6$	Mg-Cr-Ts	61.4	181[e]			114[e]					
$Fe_2Si_2O_6$	Fs	66.1	101			52			3.93	0	0
$Mg_2Si_2O_6$	En	62.66	106.7	10.9	−0.027[f]	75.93	1.6	−0.012[f]	2.95	2.69	−0.5588
$CaMgSi_2O_6$	Di	66.02	111	4.5		65	1.7		3.33	0	0
					Garnet						
$Mg_3Al_2Si_3O_{12}$	Py	113.2	172	4.85		92.25	1.6		2.31	5.96	−0.4538
$Ca_3Al_2Si_3O_{12}$	Gr	125.3	169.8	5.22	−0.0149	108.8		−0.0125	1.95	8.09	−0.4972
$Mg_3Cr_2Si_3O_{12}$	Kn	117.5									
$Fe_3Al_2Si_3O_{12}$	Alm	115.4	176.5	4.825		98.1			1.78	12.1	−0.5071
$Ca_3Cr_2Si_3O_{12}$	Uv		162			92					
					Spinel						
$FeCr_2O_4$	Chr	44.41	203			105			1.43	11.2	−0.1063
$MgAl_2O_4$	Sp	39.75	199.6	5.275	−0.015	108.2	0.44	−0.01	2.49	0	0
$MgCr_2O_4$	PChr	43.56							0.513	15.9	0
$FeAl_2O_4$	Hercy		210.3			84.4			0.977	19.4	0
					Olivine						
Mg_2SiO_4	Fo	43.63	128.8	4.63	−0.016	81.15	1.61	−0.013	2.85	10.1	−0.3842
Fe_2SiO_4	Fa	46.35	134.0	5.2	−0.025	50.7	1.50	−0.013	2.39	11.5	−0.0518

[a]Molar volumes are taken from the work of *Brey et al.* [1999].
[b]Bulk moduli represent averages of compiled data shown in Table 4.
[c]Shear moduli represent averages of compiled data shown in Table 4.
[d]Thermal expansion data are from the work of *Fei* [1995].
[e]Elastic moduli of Mg-Tschermak pyroxene end-member was determined by unmixing the elastic moduli (K_S = 115.5 GPa, G = 78.1 GPa) of a natural aluminous orthopyroxene ($En_{0.735}Fs_{0.0867}Di_{0.041}Mg\text{-}Ts_{0.122}$) from the work of *Chai et al.* [1997] (see Table 4) using the end-member elastic moduli of Diopside, Enstatite, and Ferrosilite in this table (see text for details).
[f]Values of a bronzite ($Mg_{1.6}Fe_{0.4}Si_2O_6$) are substituted here due to lack of data on mineral end-members (see Table 4). Mg-Ts (Magnesium-Tschermak pyroxene), Mg-Cr-Ts (Magnesium-Chromium-Tschermak pyroxene), Fs (Ferrosilite), En (Enstatite), Di (Diopside), Py (Pyrope), Gr (Grossular), Kn (Knorringite), Alm (Almandine), Uv (Uvarovite), Chr (Chromite), Sp (Spinel), PChr (Picrochromite), Hercy (Hercynite), Fo (Forsterite), Fa (Fayalite).

[1999], which accounts for nonideal mixing effects, was adopted exactly:

$$V_{Sp} = (1 - X_{Mg})V_{Chr} + (1 - X_{Cr})V_{Sp}$$
$$+ (X_{Mg} + X_{Cr} - 1)V_{Pch} + (1 - X_{Mg})(1 - X_{Cr})\Delta V_I$$
$$+ X_{Mg}(1 - X_{Mg})\left[W^V_{MgFe}(1 - X_{Mg}) + W^V_{FeMg}X_{Mg}\right]$$
$$+ 2X_{Cr}(1 - X_{Cr})\left[W^V_{CrAl}(1 - X_{Cr}) + W^V_{AlCr}X_{Cr}\right], \quad (1)$$

where $X_{Cr} = Cr/(Cr + Al)$, $X_{Mg} = Mg/(Mg + Fe)$, and Cr, Al, Mg, and Fe represent atomic proportions on a 4-oxygen basis. The fourth term represents the reciprocal intersite mixing term, where ΔV_I is the volume change of the reciprocal reaction

(R1) $MgAl_2O_4 + FeCr_2O_4 = FeAl_2O_4 + MgCr_2O_4$.
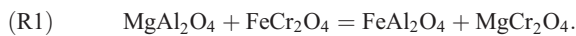
The last two terms are Margules parameterizations, which account for the nonideality of intrasite interactions.

4.2.3. Garnet

[20] Garnets typical of ultramafic rocks are assumed to have the following chemistry and stoichiometry: (Ca,Mg, Fe)₃(Cr,Al)₂Si₃O₁₂. It is assumed that Cr occurs only in the Al site. The garnet compositions can thus be described by the following components: pyrope ($Mg_3Al_2Si_3O_{12}$), grossular ($Ca_3Al_2Si_3O_{12}$), knorringite ($Mg_3Cr_2Si_3O_{12}$), and almandine ($Fe_3Al_2Si_3O_{12}$). The mixing model and molar volume parameters of *Brey et al.* [1999] were adopted exactly:

$$V^{Gt} = (X_{Mg} - X_{Cr})V_{Py} + X_{Ca}V_{Gr} + X_{Cr}V_{Kn}$$
$$+ (1 - X_{Mg} - X_{Ca})V_{Alm} + (1 - X_{Mg} - X_{Ca})X_{Cr}\Delta V_{II}$$
$$+ X_{Ca}X_{Cr}\Delta V_{III} + V^{ex}_{CaMgFe} + 2X_{Cr}(1 - X_{Cr})$$
$$\cdot \left[W^V_{AlCr}X_{Cr} + W^V_{CrAl}(1 - X_{Cr})\right], \quad (2)$$
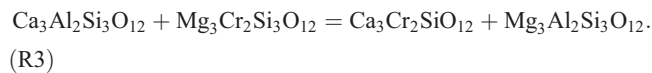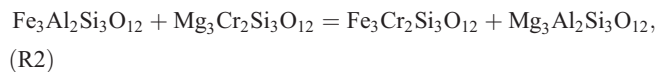
where $X_{Ca} = Ca/(Ca + Mg + Fe)$, $X_{Mg} = Mg/(Ca + Fe + Mg)$, $X_{Cr} = Cr/(Cr + Al)$, and Ca, Mg, Fe, Cr, and Al are atomic proportions on 12-oxygen basis. The fourth and fifth terms represent reciprocal mixing terms, where ΔV_{II} and

Table 3. Reciprocal Mixing Terms[a]

	Molar volume, cm³ mole⁻¹
Spinel	
W^V_{CrAl}	0.17
W^V_{AlCr}	−0.1
$W^V_{FeMg} = W^V_{MgFe}$	−0.2
Garnet	
ΔV_{II}	0.3
ΔV_{III}	0.4
$W^V_{AlCr} = W^V_{CrAl}$	0.18

[a]Data are from the work of *Brey et al.* [1999].

ΔV_{III} represent the volume changes of the following reactions:

$$Fe_3Al_2Si_3O_{12} + Mg_3Cr_2Si_3O_{12} = Fe_3Cr_2Si_3O_{12} + Mg_3Al_2Si_3O_{12},$$
(R2)

$$Ca_3Al_2Si_3O_{12} + Mg_3Cr_2Si_3O_{12} = Ca_3Cr_2SiO_{12} + Mg_3Al_2Si_3O_{12}.$$
(R3)

The last two terms account for intrasite nonidealities (Table 3).

4.2.4. Pyroxenes

[21] Pyroxenes in ultramafic rocks were assumed to have the following composition and stoichiometry: $(Ca, Mg, Fe)^{M2}(Mg, Fe, Al, Cr)^{M1}(Si, Al)_2O_6$. Ca was assumed to occur only in the larger M2 site, Al was assumed to occur both in the octahedral M1 and tetrahedral Si site, and Cr was assumed to occur only in the M1 site. Pyroxene composition can thus be described using the following end-member components: enstatite ($MgMgSi_2O_6$), ferrosilite ($FeFeSi_2O_6$), Mg-Tschermack ($MgAlAlSiO_6$), Cr-Mg-Tschermack ($MgCrAlSiO_6$), and diopside ($CaMgSi_2O_6$). The mixing model of *Brey et al.* [1999] for orthopyroxene was modified to describe clinopyroxene as well, yielding

$$
\begin{aligned}
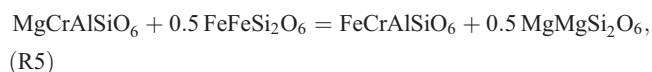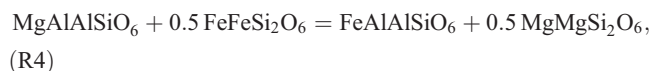V^{Px} =& \left(X^{M2}_{Mg} - X^{M1}_{Al} - X^{M1}_{Cr}\right)V_{En} + \left(1 - X^{M2}_{Mg} - X_{Ca}\right)V_{Fs} \\
&+ X^{M1}_{Al}V_{Mg-ts} + X^{M1}_{Cr}V_{Cr-ts} + X_{Ca}V_{Di} \\
&+ X^{M1}_{Al}\left(1 - X^{M2}_{Mg} - X_{Ca}\right)\Delta V_{IV} \\
&+ X^{M1}_{Cr}\left(1 - X^{M2}_{Mg} - X_{Ca}\right)\Delta V_{V} + X^{M1}_{Al}X_{Ca}\Delta V_{VI} + V^{ex},
\end{aligned}
$$
(4)

where $X^{M1}_{Al} = (Al - Cr)/2$, $X_{Cr} = Cr$, and

$$X^{M2}_{Ca} = \frac{Ca}{Mg + Fe + Ca + X^{M1}_{Al} + Cr + -1},$$

$$X^{M2}_{Mg} = \frac{Mg}{Mg + Fe}\left(1 + \frac{X^{M2}_{Ca}}{Mg + Fe - 1 + X^{M1}_{Al} + Cr}\right)^{-1},$$

and ΔV_{IV}, ΔV_{V}, and ΔV_{VI} represent the volume change for the following respective reactions:

$$MgAlAlSiO_6 + 0.5\,FeFeSi_2O_6 = FeAlAlSiO_6 + 0.5\,MgMgSi_2O_6,$$
(R4)

$$MgCrAlSiO_6 + 0.5\,FeFeSi_2O_6 = FeCrAlSiO_6 + 0.5\,MgMgSi_2O_6,$$
(R5)

$$MgAlAlSiO_6 + CaMgSi_2O_6 = CaAlAlSiO_6 + MgMgSi_2O_6.$$
(R6)
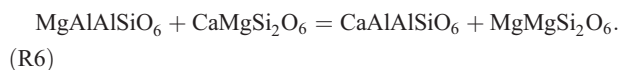
Brey et al. showed that the nonideal mixing terms for orthopyroxene are very close to zero. Mixing of end-member components was thus assumed to be ideal for clinopyroxene as well. The nonideal mixing terms, however, are shown here for completeness in case there is a need in the future to update the calculations.

4.3. Elastic Parameters and Seismic Velocities

[22] The isotropic adiabatic bulk moduli (K_S) and the shear moduli (G) of peridotites at STP conditions were calculated as follows. Elastic moduli of mineral end-members were taken from compilations by *Bass* [1995] and *Isaak et al.* [1993] and from additional literature sources; each of the data points used (and their respective literature sources) is shown in Table 4. The average values for each mineral end-member are tabulated in Table 2, which are the values used here in calculating elastic moduli of impure minerals. The K_S and G for each mineral were calculated by assuming linear additivity of the elastic parameters of the end-member mineral components, e.g., $M = \sum M_i X_i$, where M is the elastic modulus of the mineral solid solution, M_i is the elastic modulus of the mineral end-member component, and X_i is the mole fraction of the mineral end-member component. Olivine solid solution was described using only the forsterite and fayalite components. Garnet was constructed from the following components: Pyrope ($Mg_3Al_2Si_3O_{12}$), Grossular ($Ca_3Al_2Si_3O_{12}$), Uvarovite ($Ca_3Cr_2Si_3O_{12}$), and Almandine ($Fe_3Al_2Si_3O_{12}$). Spinel was constructed from Chromite ($FeCr_2O_4$), Spinel ($MgAl_2O_4$), and Hercynite ($FeAl_2O_4$) components.

[23] Pyroxenes were constructed with Enstatite ($Mg_2Si_2O_6$), Ferrosilite ($Fe_2Si_2O_6$), Diopside ($CaMgSi_2O_6$), and Mg-Tschermak ($MgAl_2SiO_6$) components. There were no elastic data available for pure Mg-Tschermak or Cr-Tschermak end-members. The elastic moduli of the Mg-Tschermak end-member was inferred from experimentally determined elastic moduli of a natural aluminous orthopyroxene [*Chai et al.*, 1997]. For a natural pyroxene having the composition $En_{0.735}Fs_{0.0867}Di_{0.041}Mg\text{-}Ts_{0.122}$ ($Al_2O_3 \sim$ 4 wt %, $CaO \sim$ 1 wt %), Chai et al. found that STP K_S and G are 115.5 and 78.1 GPa, respectively. The elastic moduli of the Mg-Tschermak end-member was extracted by "unmixing" the natural orthopyroxene of Chai et al. using the first five terms in the mixing model of equation (4) and the elastic moduli of Diopside, Enstatite, and Ferrosilite components shown in Table 2. A K_S of 181 GPa and a G of 114 GPa for the pure Mg-Tschermak end-member were obtained (compare with K_S = 107 GPa and G = 75.9 GPa for pure Enstatite; Table 2). These values are considerably higher than those of Tschermak-free orthopyroxenes (see Table 2), indicating that Al substitution in pyroxenes may have a significant effect on elastic moduli. For garnet-facies peridotites, the Al_2O_3 content in clinopyroxenes and orthopyroxenes is small (<2 wt %; <4% Mg-Ts), and therefore there is only a small effect on the elastic moduli caused by the incorporation of Mg-Tschermak component. However, for spinel-facies peridotites, the Al_2O_3 content ranges between 2 and 6 wt % for orthopyroxene and 2 and 8 wt % for clinopyroxene. For spinel-facies peridotites, failure to account for the Mg-Tschermak component will result in an underestimate of seismic velocities by ~3%. Additional effects may be caused by the incorporation of Cr-Tschermak component, but lack of elastic data on Cr-bearing pyroxenes prevents its consideration in this paper. However, ignoring this component may not introduce significant error into this

Table 4. Elastic Properties of Mineral End-Members[a]

	STP Density (ρ), g cm^{-3}	Isotropic Adiabatic Bulk Modulus			Isotropic Shear Modulus			Reference
		K_S, GPa	dK_S/dP	dK_S/dT, GPa °K^{-1}	G, GPa	dG/dP	dG/dT, GPa °K^{-1}	
				Pyroxene				
Hedenbergite (CaFeSi$_2$O$_6$)	3.657	120			61			[Kandelin and Weidner, 1988]
Ferrosilite (Fe$_2$Si$_2$O$_6$)	4.002	101			52			[Bass and Weidner, 1984]
Bronzite (Mg$_{1.6}$ Fe$_{0.4}$Si$_2$O$_6$)		112	10.80		63	2.06		[Webb and Jackson, 1993]
		103.5	9.59	−0.027	75.5	2.38	−0.012	[Frisillo and Barsch, 1972]
Aluminous Enstatite (Mg$_{1.63}$Fe$_{0.17}$Ca$_{0.04}$ Al$_{0.24}$Si$_{1.89}$O$_{16}$)	3.306	115.5			78.1			[Chai et al., 1997]
Enstatite (Mg$_2$Si$_2$O$_6$)	3.194	108			76.8			[Jackson et al., 1999]
	3.198	108			76			[Weidner et al., 1978]
	3.180	104	10.9		75	1.6		[Flesch et al., 1998]
Ave		106.7	10.9		75.9	1.6		
STD		4.62			1.8			
Diopside (CaMgSi$_2$O$_6$)	3.310	114			64.9			[Aleksandrov et al., 1964]
	3.289	108			65.1			[Levien et al., 1979]
Ave		111			65			
STD		8.49			0.28			
				Olivine				
Fayalite (Fe$_2$SiO$_4$)	4.380	127.9	5.20	−0.030	50.3	1.50	−0.013	[Graham et al., 1988]
	4.400	137.9		−0.021	50.9		−0.011	[Sumino, 1979]
Ave		134	5.20	−0.024	50.7	1.50	−0.013	
STD								
Forsterite (Mg$_2$SiO$_4$)			4.20			1.40		[Duffy et al., 1995]
	3.226	128.7	4.19			1.70		[Yoneda and Morioka, 1992]
	3.222	128.8		−0.016	81.8		−0.014	[Isaak et al., 1989]
	3.225	128.8		−0.016	81.2		−0.013	[Suzuki et al., 1983]
	3.220	129.2		−0.016	81.2		−0.014	[Sumino et al., 1977]
	3.221	129.1	4.97	−0.018	81.6	1.82	−0.014	[Graham and Barsch, 1969]
	3.224	128.9	5.37	−0.015	81.1	1.80	−0.013	[Kumazawa and Anderson, 1969]
		128	4.44		80	1.32		[Li et al., 1996, 1998]
Ave		128.8	4.63	−0.016	81.1	1.61	−0.013	
STD		0.8	1.06	0.0019	1.3	0.47	0.0008	
				Garnet				
Uvarovite (Ca$_3$Cr$_2$Si$_3$O$_{12}$)	3.850	162			92			[Bass, 1986]
Grossular (Ca$_3$Al$_2$Si$_3$O$_{12}$)	3.597	167.8		−0.015	107		−0.013	[Isaak et al., 1992] (1% andradite)
	3.607	169.1			110.6			[Babuska et al., 1978]
		174	4.25					[Weaver et al., 1976]
		168	6.20					[Olijnyk et al., 1991]
		170	5.20					[Zhang et al., 1999]
Ave		169.7	5.22	−0.01	108.8		−0.01	
STD		5.0	1.95					
Pyrope (Mg$_3$Al$_2$Si$_3$O$_{12}$)	3.570	171	5.30		92	1.60		[Chen et al., 1999]
		171	4.40					[Zhang et al., 1998]
		173			92.5			[Babuska et al., 1978]
Ave		172	4.85		92.3	1.60	−0.013	
STD		2.3			0.71			
Almandine (Fe$_3$Al$_2$Si$_3$O$_{12}$)	4.325	177.9			98.1			[Babuska et al., 1978]
		168	5.45					[Takahashi and Liu, 1970]
		175	1.50					[Sato et al., 1978]
		185	4.20					[Zhang et al., 1999]
Ave		176.5	3.72					
STD		7.0	2.02					
				Spinel				
Chromite (Fe$_2$Cr$_2$O$_4$)	5.090	203			105			[Hearmon, 1984]
Hercynite (FeAl$_2$O$_4$)	4.280	210.3			84.40			[Wang and Simmons, 1972]
Spinel (MgAl$_2$O$_4$)	3.585	197.39		−0.014	107.8		−0.008	[Suzuki et al., 2000]
	3.574	210.1		−0.015	108.3		−0.012	[Cynn et al., 1993]
	3.578	197.9	5.66		108.5	0.36		[Yoneda, 1990]
	3.578	197.4	4.89	−0.015	108.8	0.51		[Chang and Barsch, 1969]
	3.581	195			107.5			[Lewis, 1966]
				−0.016			−0.009	[Liu et al., 1975]
Ave		199.6	5.28	−0.015	108.2	0.44	−0.010	
STD		6.0	0.54	0.001	0.5	0.11	0.003	

[a]The majority of the above parameterizations are directly from compilations by *Bass* [1975] and *Isaak* [2001].

study because (1) it is a small component in most pyroxenes and (2) its concentration in pyroxenes remains relatively constant over a wide range in the composition of the host bulk rock.

[24] Assuming that the bulk rock is an isotropic mixture of the mineral constituents, its elastic moduli were calculated using two theoretical mixing models, the Voigt-Reuss-Hill (VRH) average and the Hashin-Shtrikman (HS) average. A good review of the application of these mixing models to earth materials is given by *Watt et al.* [1976]. The Hashin-Shtrikman average is reported here as it produced tighter bounds on the elastic moduli. For completeness, the relevant equations by Watt et al. are shown here. The upper (K_+^*) and minimum (K_-^*) bounds for the bulk modulus are

$$K_-^* = K_1 + [A_1/(1 + \alpha_1 A_1)]$$
$$K_+^* = K_n + [A_n/(1 + \alpha_n A_n)], \tag{7}$$

where K_1 represents the smallest of the n moduli, K_n is the largest moduli, and

$$\alpha_1 = -3/(3K_1 + 4G_1), \tag{8a}$$

$$\alpha_n = -3/(3K_n + 4G_n), \tag{8b}$$

$$A_1 = \sum_{i=2}^{n} \frac{X_i}{(K_i - K_1)^{-1} - \alpha_1}, \tag{8c}$$

$$A_n = \sum_{i=1}^{n-1} \frac{X_i}{(K_i - K_n)^{-1} - \alpha_n}. \tag{8d}$$

For the shear modulus, the maximum G_+^* and minimum G_-^* bounds are

$$G_-^* = G_1 + [B_1/(1 + \beta_1 B_1)]/2, \tag{9a}$$

$$G_+^* = G_n + [B_n/(1 + \beta_n B_n)]/2, \tag{9b}$$

where G_1 is the smallest of the n shear moduli, G_n is the largest, and

$$\beta_1 = -3[K_1 + 2G_1]/[5G_1(3K_1 + 4G_1)], \tag{10a}$$

$$\beta_n = -3[K_n + 2G_n]/[5G_n(3K_n + 4G_n)], \tag{10b}$$

$$B_1 = \sum_{i=2}^{n} \frac{X_i}{[2(G_i - G_1)]^{-1} - \beta_1}, \tag{10c}$$

$$B_n = \sum_{i=1}^{n-1} \frac{X_i}{[2(G_i - G_n)]^{-1} - \beta_n}. \tag{10d}$$

[25] Compressional (V_P) and shear (V_S) velocities at STP were calculated using the bulk densities and HS averages of

the bulk-rock elastic parameters. The largest uncertainty (shown in figures) in seismic velocity determinations was estimated by propagating the uncertainties in mineral modes, elastic moduli, and density.

4.4. Estimation of Errors

[26] Errors on the elastic moduli calculated for natural minerals were estimated by propagating the errors (two standard deviations) for the elastic moduli of the mineral end-member components. Mineral density errors were negligible compared to the possible errors in estimating mineral modes. The errors on estimated mineral modes are difficult to quantify. Ideally, the error on mineral modes can be calculated by propagating the uncertainties in mineral compositions and bulk-rock compositions. These uncertainties are controlled by heterogeneity in the mineral and in the bulk rock rather than by analytical uncertainties, which are relatively small. Mineral-scale heterogeneity, however, is seldom fully quantified in most of the published studies from which the data in this study are derived. The approximate errors on mineral mode calculations were instead estimated by calculating the misfit between the measured bulk composition and that determined from the calculated mineral modes. In so doing, it is assumed that any misfit reflects sample or mineral heterogeneity. Samples with misfits greater than 0.7% were omitted. The "maximum" error on estimated seismic velocity was determined by propagating the maximum estimated error (0.7%) on mineral modes and elastic moduli. A linear regression was applied to fit the density and seismic velocity data to corresponding compositional parameters (e.g., Mg# and olivine mode); no weighting of data points was applied due to the difficulty in estimating errors.

5. Results

5.1. Mineral Modes

[27] Calculated mineral modes for two samples described previously in the literature are shown in Figures 5a and 5b. In general, there is good agreement with *Boyd and McAllister*'s [1976] calculations, as should be expected because the approaches are similar. The agreement with *Jordan*'s [1979] calculations is not so good. In the case of PHN1569, a harzburgite, Jordan's approach results in much higher garnet contents. This is probably due to the fact that the orthopyroxenes in PHN1569 account for a nonnegligible amount of the Al in the bulk (41% of the bulk Al_2O_3) so that Jordan's assumption of zero Al_2O_3 content in orthopyroxene results in an overestimation of garnet content. In PHN1611, orthopyroxenes account for only 3% of the bulk Al_2O_3 content, which explains why, in this case, Jordan's calculated modes are in agreement.

5.2. Densities

[28] Figures 5b and 5c compare our calculated mineral and bulk densities with the calculated densities of *Jordan* [1979] and the measured mineral densities of *Boyd and McAllister* [1979]. The mineral densities calculated here agree better than Jordan's densities with the measured mineral densities of Boyd and McAllister. However, for reasons not understood, the garnet and clinopyroxene densities for PHN1569 calculated here and by Jordan are about 1% higher than the measured garnet and clinopyroxene
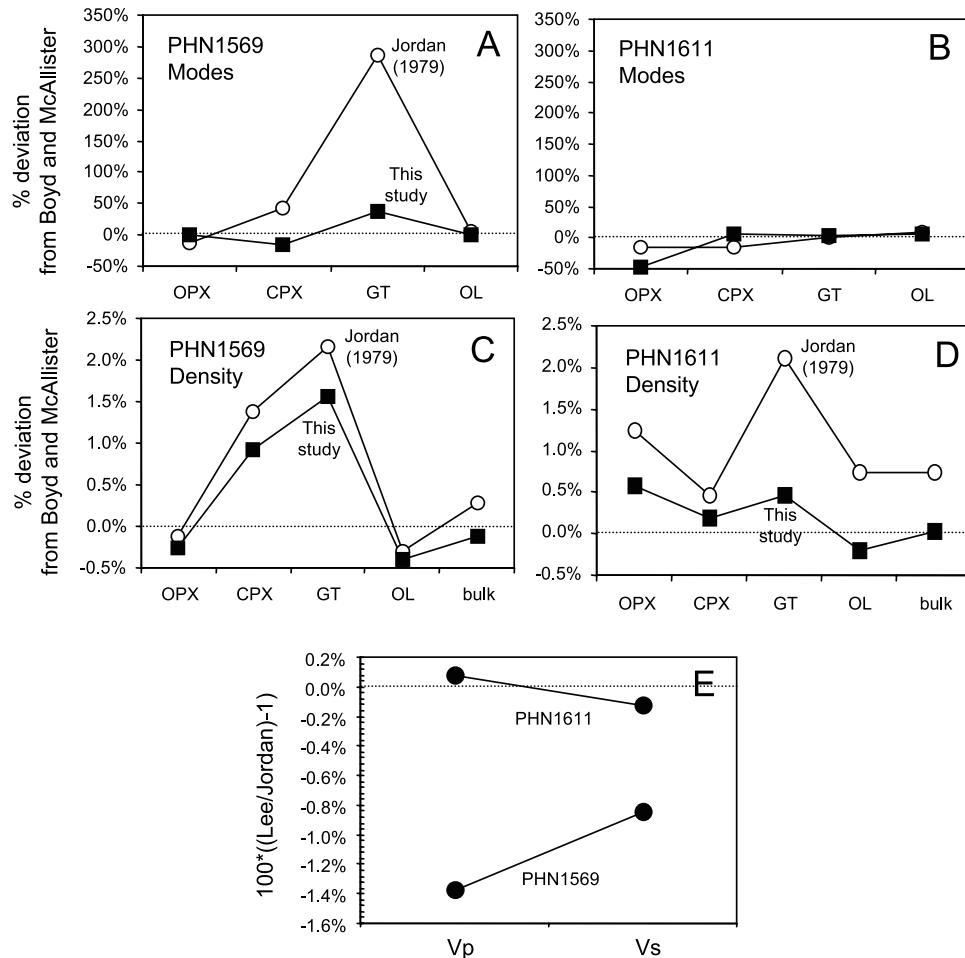
Figure 5. (a, b) Comparison of calculated modes for two samples examined by *Jordan* [1979], *Boyd and McAllister* [1976], and this study (expressed as % deviation from the work of *Boyd and McAllister* [1976]); OPX, orthopyroxene; CPX, clinopyroxene; GT, garnet; OL, olivine; bulk, whole rock. (c, d) Comparison of density calculations at STP conditions (standard temperature and pressure; 25°C, and 1 atm). (e) Comparison of seismic velocity calculations by *Jordan* [1979] and this study.

densities of Boyd and McAllister. Nevertheless, the bulk densities calculated here agree well with the bulk densities of Boyd and McAllister. Jordan's bulk densities for PHN1569 and PHN1611 are overestimated because of an overestimation of garnet mode in the former and an over-estimation of garnet density in the latter.

[29] Figure 6 shows how STP bulk density (g cm^{-3}) correlates with garnet (Figure 6a) and spinel (Figure 6b) mode. In Figure 6a, garnet-peridotites have been given different symbols in order to denote the bulk Mg# of the peridotite (large symbols for Mg# > 91, small symbols for Mg# < 91). When the garnet-peridotite data are taken as a whole, bulk densities roughly correlate with garnet mode. This is an expected result as garnet, being the densest phase in garnet-peridotites, controls the bulk density. However, if only garnet-peridotites with Mg# > 91 are considered, the correlation with garnet mode is poor. This is due to the fact that at high Mg#s, garnet mode is reduced, and the variation in orthopyroxene/olivine ratio is likely to exert more of a control on bulk density.

[30] Figure 6b shows how density varies as a function of spinel mode in spinel-facies peridotites and in garnet-facies

spinel-peridotites. As defined earlier, garnet-facies spinel-peridotites represent peridotites derived from pressures greater than ~1.5 GPa but otherwise contain Cr-rich spinel. As expected, when the data are taken collectively, there appears to be a rough positive correlation between bulk density and spinel mode. The garnet-facies spinel-perido-tites tend to be slightly denser than spinel-facies peridotites owing to the fact that Cr-rich spinel is denser than alumi-nous spinel.

[31] Figures 7a and 7b show bulk densities of garnet-peridotites and garnet-facies spinel-peridotites as a function of bulk Mg# and olivine Mg#. There is a strong negative correlation between bulk density and the two Mg#s. Re-gression and fit parameters are shown in Table 5. This negative correlation is mainly due to the fact that mineral densities are correlated with Fe content, and to a lesser extent, to the fact that garnet mode decreases with increas-ing Mg#. *Jordan's* [1979] empirical correlation is also shown for reference. The correlation presented here differs slightly from Jordan's but is to within error the same. This correlation differs from a previous attempt by this author to determine a density-Mg# empirical fit on natural samples
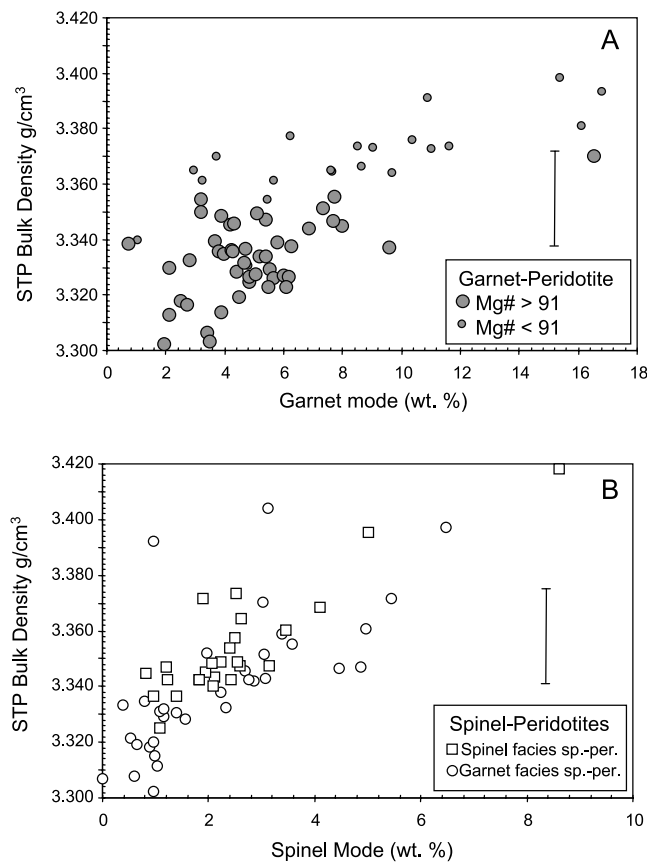
Figure 6. (a) STP bulk density calculations of garnet-peridotites versus garnet mode; vertical bar represents the estimated largest 2σ error for density calculations. (b) Same as in Figure 6a, but spinel-facies spinel-peridotites and garnet-facies spinel-peridotites have been superimposed. Error bar as in Figure 6a.

[*Lee et al.*, 2001]. In that particular paper, the density data set was limited to garnet-facies Cr-rich spinel-peridotites, a few garnet-peridotites, and some Fe-rich dunites from Tanzania. The combination of Fe-rich dunites and garnet-facies spinel-peridotites resulted in a less negative $d\rho/d$Mg# because the lack of garnet and clinopyroxene in the Fe-rich dunites suppressed the increase in density with decreasing Mg#; these Fe-rich dunites have been omitted from this paper in order to focus on the density effects of residual peridotites only.

[32] Figures 7c and 7d are reproduced from Figures 7a and 7b after adding the spinel-facies peridotites. It can be seen that these peridotites, owing to their aluminous (as opposed to Cr-rich) spinels, have slightly lower densities than the garnet-facies spinel-peridotites at a given Mg#. There appears to be a rough negative correlation between bulk composition and Mg# for spinel-facies peridotites.

5.3. Seismic Velocities

[33] Figures 8a–8d show how STP elastic moduli (K_S and G) calculated from mineral end-member moduli for natural minerals compare with direct experimental measurements on natural minerals. In most cases, the calculated moduli agree with the direct observations to within error. For the

purposes of this paper, it is assumed that the calculated elastic moduli provide a reasonably accurate prediction of the elastic moduli of natural samples in the absence of direct experimental observation of all natural compositions of interest. The most important feature of Figure 8 is that over the compositional range of natural residual peridotites (Mg# $\sim$ 88–93), there is a much stronger dependence of shear modulus (G) on Mg# than there is for bulk modulus (K_S); over the compositional range of interest, G varies by over 2% whereas K_S varies by no more than 1%.

[34] The STP V_P and V_S calculated using these elastic moduli and density determinations are shown in Figures 9–13. In Figures 9–13, only garnet-facies peridotite data have been linearly regressed. Linear regression parameters and their associated standard errors (2σ) are shown in Table 5. No attempt to regress the spinel-facies data was made due to the small number of data points. Figure 9 shows how V_S varies with bulk Mg# for garnet-facies peridotites and spinel-facies peridotites. It can be seen that there is a strong positive correlation of V_S on bulk Mg# for garnet-facies peridotites but only a weak dependence for spinel-facies peridotites. Shear wave velocities vary by $\sim$2.5% between Mg# 86 and 94. There appears to be no correlation between V_S and olivine mode (Figure 10a). In contrast to V_S, there is almost no correlation between V_P and bulk Mg# (Figure 11). This is due to the stronger dependence of shear modulus on Mg# than bulk modulus on Mg#. Instead, there appears to be a weak positive correlation between V_P and olivine mode (Figure 10b) due to the different K_S values of olivine and orthopyroxene at STP conditions. However, at elevated pressures and temperatures, olivine and orthopyroxene will have similar K_S due to the fact that the pressure derivative of K_S (dK_S/dP) for orthopyroxene is about two times higher than in olivine [*Webb and Jackson*, 1993]. For example, using the pressure and temperature derivatives of K_S shown in Table 2, it can be seen that K_S for forsteritic olivine is 132.8 GPa and for enstatitic orthopyroxene is 128.8 GPa at 5 GPa and 1200°C (compare with 128.8 for forsterite and 106.7 for enstatite at STP conditions). Thus it is likely that the weak correlation between V_P and olivine mode at STP conditions (Figure 10b) disappears completely at upper mantle conditions.

[35] It is important to note that the pressure and temperature derivatives of the elastic moduli of the mineral end-member components are very similar (Tables 2 and 4) and the entire compositional range in upper mantle peridotites investigated here is small (Mg# = 86–94). Therefore the chemical derivatives (d/dMg#) of the elastic moduli derived here for STP conditions hold at elevated pressure and temperature.

6. Discussion
6.1. Prospects and Limitations of Using Seismic Velocities to Detect Upper Mantle Compositional Variations

[36] Figures 12 and 13 and Table 5 show the following STP total differentials for garnet-facies peridotites: $\frac{d \ln \rho}{d\text{Mg#}}$, $\frac{d \ln V_P}{d\text{Mg#}}$, $\frac{d \ln V_S}{d\text{Mg#}}$, and $\frac{d(V_P/V_S)}{d\text{Mg#}}$, where Mg# = $100 \times$ Mg/(Mg + Fe). Only garnet-facies peridotites are included in this calculation as the data set for spinel-facies peridotites is too small and too scattered to construct meaningful compositional
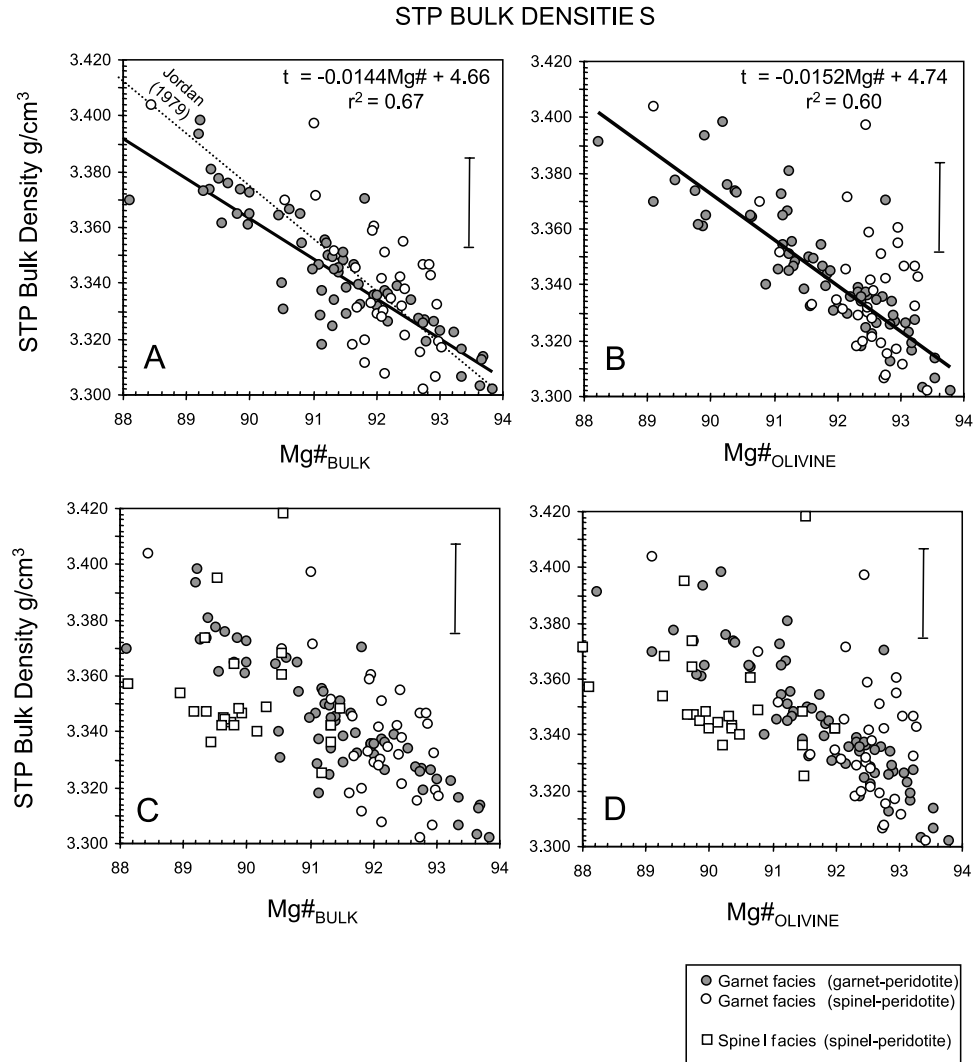
STP BULK DENSITIES

Figure 7. (a, b) STP bulk densities versus Mg# = 100 × Mg/(Mg + Fe) for garnet-facies peridotites; Mg# is expressed in the bulk (Figure 7a) or in olivine (Figure 7b). Vertical bar in Figures 7a and 7b represents the estimated largest 2σ error for density calculations. Thick solid line in Figures 7a and 7b represents regression through all of the data (regression parameters shown in upper right-hand corner). The density-Mg# parameterization of *Jordan* [1979] is also shown for reference. (c, d) Identical to Figures 7a and 7b, but with spinel-facies peridotites superimposed.

parameters. These total differentials express the entire compositional variation of density and seismic velocity in natural peridotites in terms of Mg#. Clearly, other variables besides Mg# also control density and seismic velocity (e.g., mineral modes), but some of these variables are correlated with Mg# and/or exhibit only minimal control relative to Mg#. Thus the effect of other variables has been incorporated into the total differentials with respect to Mg#. Expressed in this manner, these total differentials should simplify the compositional inputs into various geophysical and geodynamic models. It is assumed that total differentials calculated at STP conditions are relatively constant over upper mantle conditions (although the absolute values of densities and seismic velocities obviously change as a function of P and T).

[37] The question that arises is whether densities and seismic velocities are meaningfully sensitive to composi-

tion. Figures 13a and 13c indicate that density and V_S are strongly negatively and positively correlated with Mg#, respectively. Figure 12 shows that V_P/V_S is negatively correlated with Mg#. In contrast, V_P exhibits no correlation with Mg# and should be considered useless in determining compositional variations in mantle peridotites.

Table 5. Garnet-Facies Peridotites[a]

	a	SE	b	SE	R^2
$\rho = a\,(\text{Mg#}) + b$	−0.0144	±0.0010	4.66	±0.091	0.67
$V_S = a\,(\text{Mg#}) + b$	0.0143	±0.0009	3.53	±0.084	0.71
$V_P = a\,(\text{olivine mode}) + b$	0.00232	±0.00029	8.13	±0.021	0.39
$\ln \rho = a\,(\text{Mg#}) + b$	−0.00431	±0.00030	1.60	±0.030	0.67
$\ln V_S = a\,(\text{Mg#}) + b$	0.00296	±0.00019	1.31	±0.018	0.71
$V_P/V_S = a\,(\text{Mg#}) + b$	−0.00407	±0.00038	2.09	±0.035	0.54

[a]Mg# = 100 × Mg/(Mg + Fe)$_\text{bulk}$, olivine mode = wt %, V = km s^{-1}, ρ = g cm^{-3}.
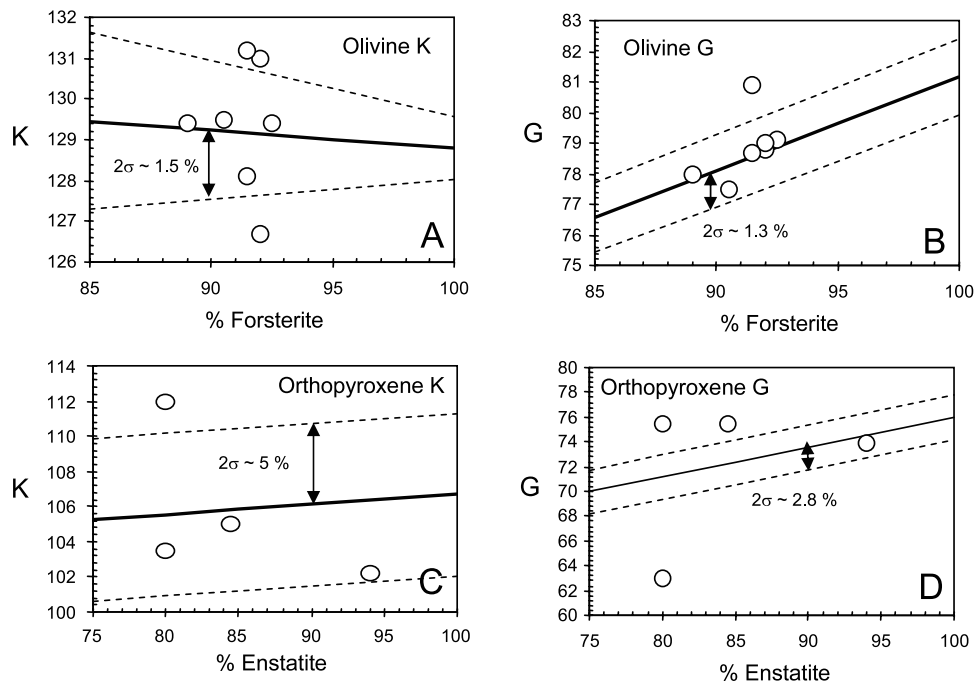
OBSERVED AND CALCULATED MINERAL ELASTIC MODULI

Figure 8. Comparison between observed and calculated mineral elastic moduli at STP conditions. (a) Isotropic adiabatic bulk modulus K_S (GPa) of olivine versus % forsterite content (% forsterite = molar $100 \times Mg/(Mg + Fe)$ in olivine); symbols represent actual experimental data on natural samples; thick solid line represents predicted value based on linear average of end-member compositions; dotted lines define the 2σ error resulting from uncertainties in the end-member moduli. (b) Shear modulus G (GPa) of olivine versus % forsterite content. (c) Adiabatic isotropic bulk modulus K_S of orthopyroxene versus % enstatite content (% enstatite = molar $100 \times Mg/(Mg + Fe)$ in orthopyroxene). (d) Shear modulus G of orthopyroxene versus % enstatite content.

[38] In Figure 14a, the relative importance of Mg# and temperature on V_S and V_P/V_S for garnet-facies peridotites is shown, where V_S and V_P at different temperatures have been estimated using existing experimental data on mineral thermal expansivities [*Fei*, 1995] and elastic moduli after correction for temperature using the first temperature derivatives of the bulk moduli (Table 2). It is found that dV_S/dT is approximately -0.00033 km s^{-1} °C^{-1}. Combined with dV_S/dMg# = 0.0150 (Figure 9a and Table 5), it can be shown that the relative effects of Mg# and temperature on a change in V_S is given by ΔMg# $\sim -0.022\ \Delta T$. This means that an $\sim$1% increase in V_S could be due to either an "increase" in Mg# by five units (e.g., from fertile lherzolite (Mg# = 88) to refractory harzburgite (Mg# = 93)) or a "decrease" in temperature by $\sim$220°C. It is thus concluded that although V_S is sensitive to compositional variations, considerable care must be taken to separate the effects of temperature. In cases where xenolith thermobarometry or surface heat flow measurements provide an independent estimate of temperature at depth, it may be possible to use V_S anomalies alone to infer bulk composition variations. An important corollary of this study is that variations in bulk Mg# of garnet-facies peridotites impose larger relative perturbations in V_S ($\sim$2.5%) than in V_P ($\sim$2%). This means that, for a given pressure and temperature, any variation in the bulk Mg# of a garnet-facies peridotite that is significant enough to yield a V_P perturbation should yield a larger
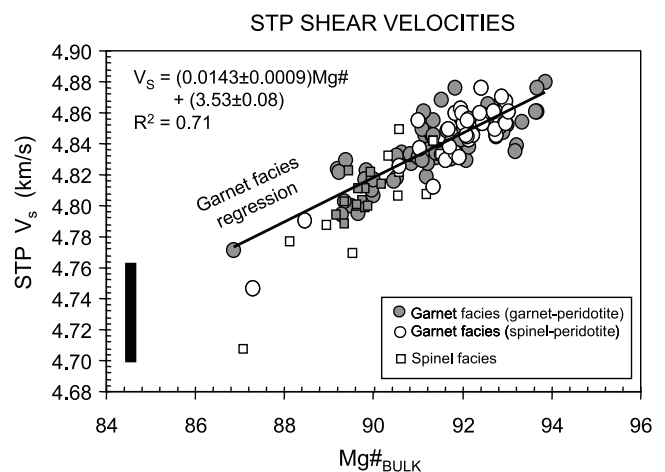

Figure 9. STP bulk shear wave velocities (V_S) versus Mg# for garnet and spinel-facies peridotites. Solid regression line is for garnet-facies peridotites only (garnet-peridotites and garnet-facies spinel-peridotites). Black vertical bar represents the estimated largest 2σ error on seismic velocity calculations.
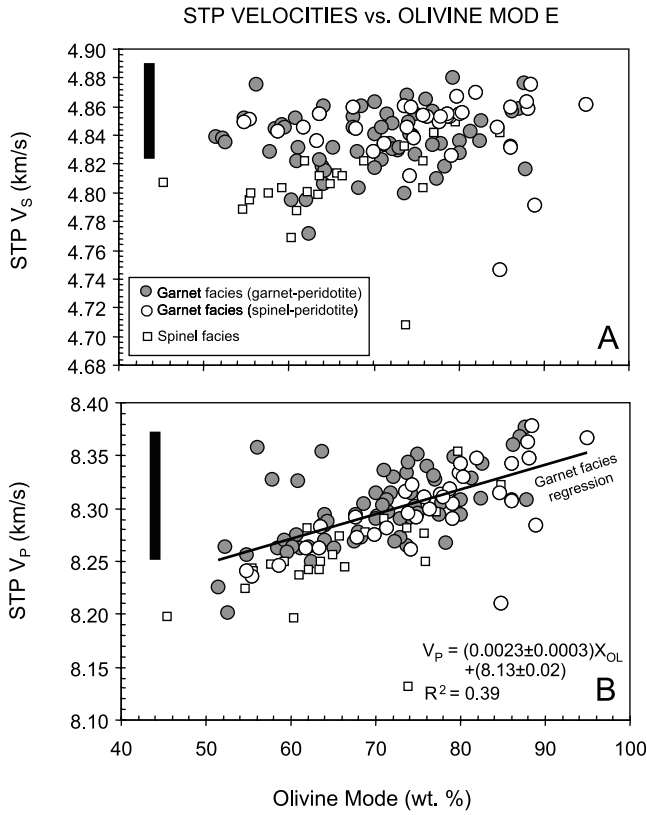
STP VELOCITIES vs. OLIVINE MOD E

Figure 10. (a) STP bulk shear wave velocities and (b) P wave velocities versus olivine mode. Regression line in Figure 10b is for garnet-facies peridotites only. Black vertical bar represents the estimated largest propagated 2σ error on seismic velocity calculations.

perturbation in V_S (assuming no melt or metasomatic phases).

[39] Along these lines, it appears that the V_P/V_S ratio may prove useful in detecting compositional variations. Figure 14b shows how this ratio varies as a function of temperature (at constant pressure) and Mg# "in the absence of a melt phase or incipient melting" (e.g., below the solidus). The temperature dependence of V_P/V_S is very

STP BULK P-WAVE VELOCITIES
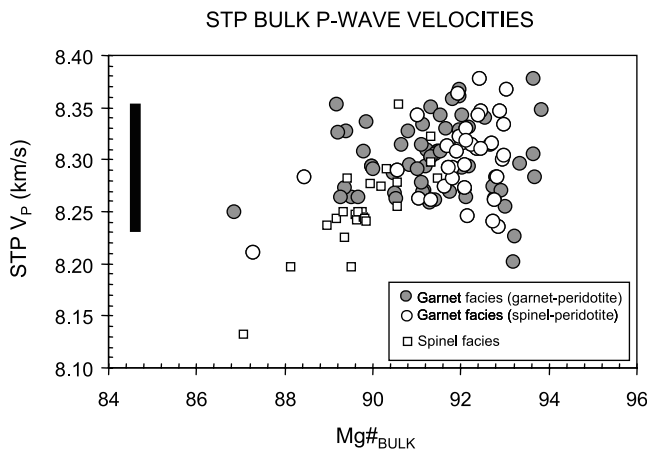
Figure 11. STP bulk P wave velocities (V_P) versus bulk Mg#. Black vertical bar represents error as in Figure 10.

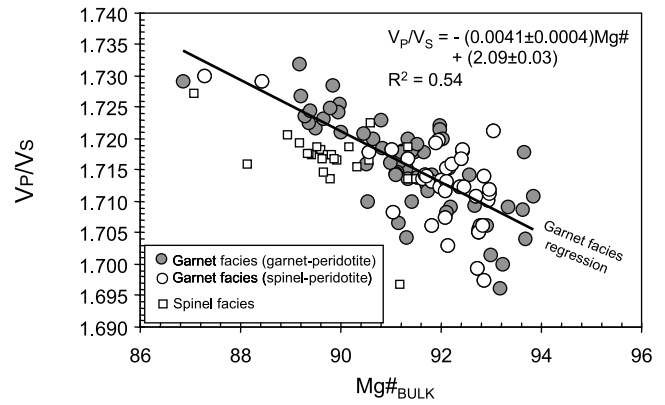**Figure 12.** The ratio V_P/V_S at STP conditions plotted against bulk Mg#. Regresion line is for garnet-facies peridotites only.
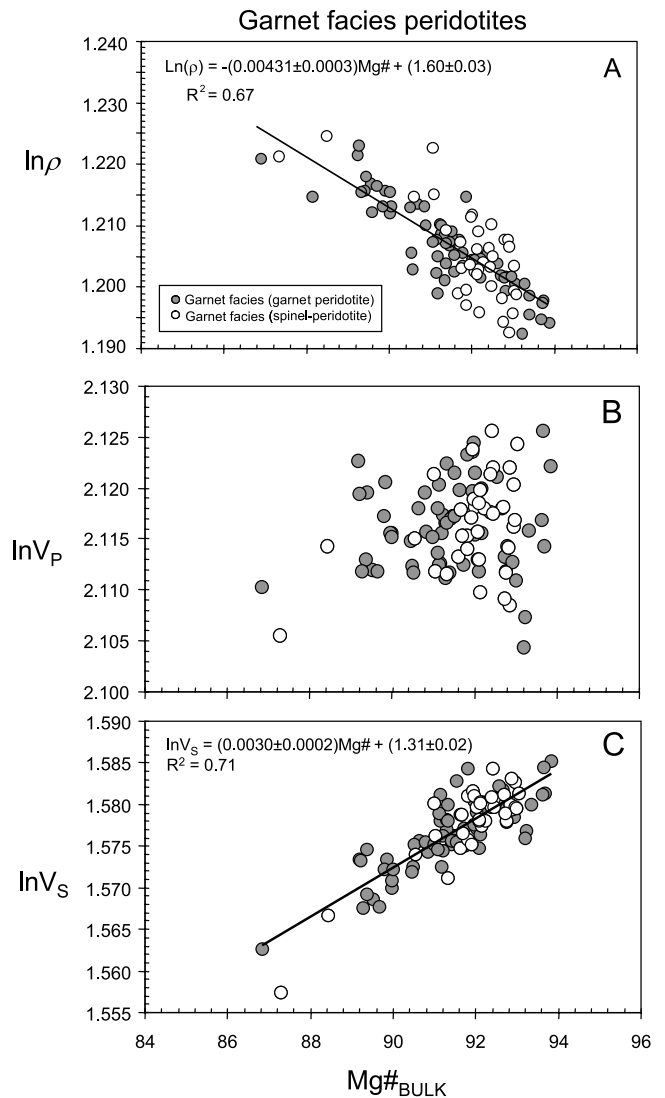
Garnet facies peridotites

Figure 13. Natural logarithm of STP density and seismic velocities versus bulk Mg# for garnet-facies peridotites only. (a) Natural logarithm of density, ln ρ, versus Mg#. (b) Natural logarithm of P wave velocity (ln V_P) versus Mg#. (c) Natural logarithm of shear wave velocity (ln V_S) versus Mg#. Regression lines are through all data.

A V_S in garnet facies

Mg#

93

90

87

V_S (% deviation)

B V_P/V_S in garnet facies

89

Mg#

91

93

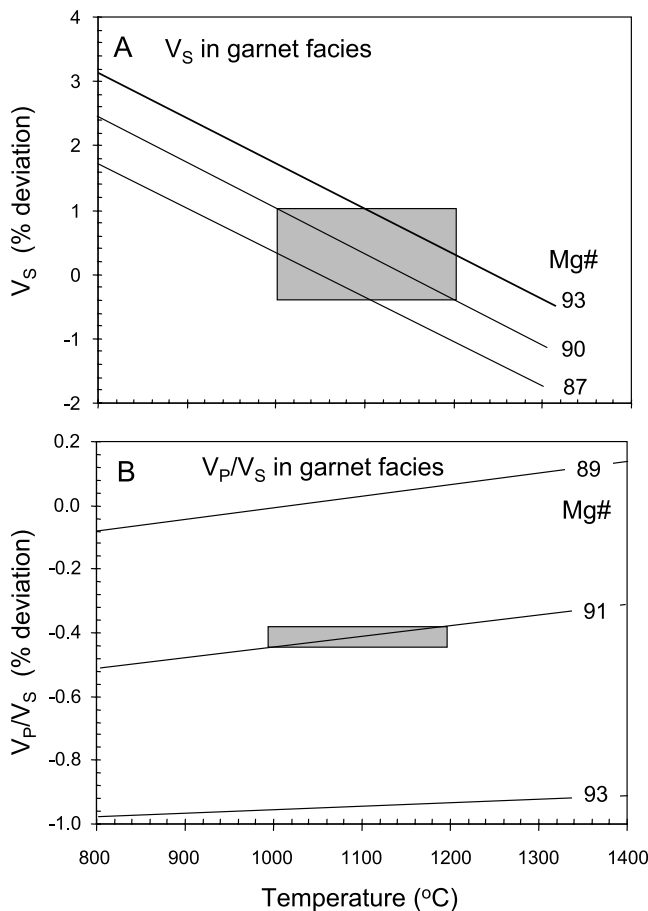V_P/V_S (% deviation)

Temperature (°C)

Figure 14. (a) Percent relative deviation of shear wave velocity (V_S) plotted against temperature and contoured for different bulk Mg#s using the V_S-Mg# parameterization given in Table 5. Shaded box in Figure 14a represents the change in Mg# that gives an equivalent change in V_S caused by a temperature difference of 200°C. (b) Percent relative deviation in V_P/V_S as a function of temperature and contoured for different bulk Mg#s. Shaded box in Figure 14b represents the change in Mg# that gives an equivalent change in V_P/V_S caused by a temperature difference of 200°C.

small (<0.04%/100°C) compared to the dependence on Mg# (~1.7%/Mg# unit). The relative effects of temperature and Mg# change on V_P/V_S is roughly ΔMg# ~ -0.1 ΔT. It can be seen from Figure 12b that this ratio is much more sensitive to composition than it is to temperature.

[40] Recent studies have observed small velocity perturbations within cratonic lithospheric mantle [*James et al.*, 2001; *Shirey et al.*, 2002]. James et al. report 1% perturbations in V_P within the South African cratonic lithospheric mantle, which was interpreted by Shirey et al. to be due to compositional differences within the South African lithospheric mantle. Shirey et al. observe that the low V_P regions coincide with the presence of eclogitic- and lherzolitic-type diamond inclusions, whereas the remainder of the lithospheric mantle is characterized by high V_P and harzburgitic inclusions. They therefore suggest that the low V_P regions are associated either with a locally refertilized lithospheric

mantle (yielding a decrease in bulk Mg# by the infiltration of melts) or the presence of eclogite. On the basis of the study presented herein, it is not likely that refertilization of a refractory peridotite (e.g., a harzburgite with Mg# of 93) to yield lherzolitic compositions within the range of primitive-type mantle (Mg# $\sim$ 88) is capable of significantly lowering V_P (e.g., Figure 11a). As just discussed, changes in bulk Mg# result in a larger decrease in V_S than in V_P, which suggests that this particular velocity anomaly is not due to a decrease in bulk Mg# alone. It is important to note that in the same study [*James et al.*, 2001; *Shirey et al.*, 2002], the region of significant V_P perturbation was not accompanied by any significant V_S perturbation. As suggested by Shirey et al., other possibilities, such as the presence of garnet pyroxenite and/or eclogites, should be investigated. However, given the high bulk and shear modulus of garnet, too much garnet will result in very large positive velocity perturbations.

6.2. Density of Lithospheric Mantle

[41] The density-Mg# correlation in Figure 7a can be used to determine whether cratonic lithospheric mantle is neutrally buoyant, as suggested by *Jordan* [1978, 1988]. Jordan recognized that continental lithosphere is thicker than oceanic lithosphere, owing to the colder thermal state of the former. The colder thermal state of continental lithospheric mantle should result in a mass excess due to the effects of thermal contraction. However, continental lithospheres appear to be more stable than oceanic lithospheres, implying paradoxically that continental lithospheric mantle must be stabilized despite their colder temperatures. *Jordan* [1978, 1988] hypothesized that continental lithospheric mantle was composed of refractory peridotite, which is intrinsically less dense than asthenospheric mantle due to previous extraction of meltable components. Jordan formalized this hypothesis into the "isopycnic hypothesis," which states that the compositional buoyancy of the lithospheric mantle offsets the negative thermal buoyancy associated with the lithosphere's colder temperatures:

$$\frac{\Delta\rho_{Mg\#}}{\rho_0} = -\alpha\Delta T_Z, \qquad (11)$$

where $\Delta\rho_{Mg\#}/\rho_0$ is the compositional buoyancy term relative to a reference state (the asthenospheric mantle), α is the thermal expansivity, and ΔT_Z is the temperature difference between the continental lithospheric mantle and the athenosphere at a particular depth Z. In Figure 15a, xenolith thermobarometric data from several literature sources are shown along with a geotherm appropriate for a surface heat flow of 40 mW m^{-2} [*Rudnick et al.*, 1993] and a 1350°C potential adiabat (assuming a 15°C km^{-1} gradient). The 40 mW m^{-2} geotherm is believed to be typical of Archean cratons and is broadly consistent with the xenolith thermobarometry [*Rudnick et al.*, 1993]. In Figure 15a, ΔT_Z would represent the difference in temperature between these two curves at a given depth. Figure 15b shows what $\Delta\rho_{Mg\#}/\rho_0$ is required to be in order for the lithospheric mantle to be neutrally buoyant at every depth, given a 40 mW m^{-2} continental geotherm.

[42] The empirical relationship between bulk density and bulk Mg# in Figure 7a ($\rho = -0.0144$ Mg# + 4.66; cf., $\rho =$
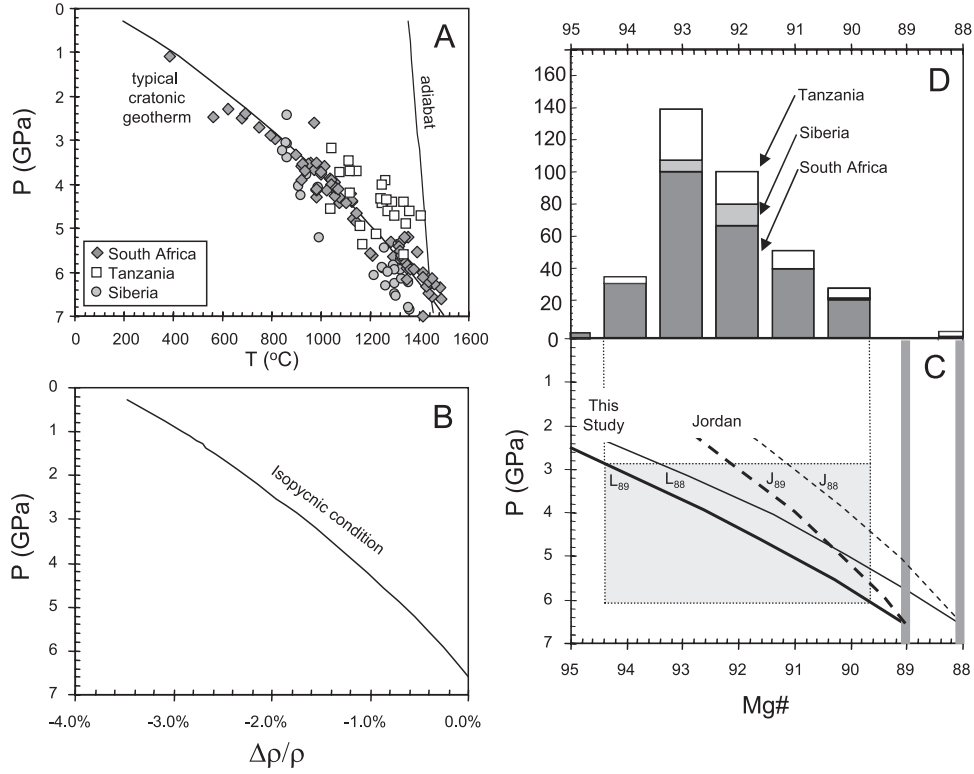
Figure 15. (a) Pressure versus temperature plot; vertical line represents a 1350°C potential adiabat, characteristic of asthenospheric mantle; curved line represents a model geotherm that fits a 40 mW m^{-2} surface heat flow constraint and average crustal heat production; data symbols represent equilibration pressures and temperatures of individual xenolith samples determined by thermobarometric measurements (all from Archean cratons). (b) Relative (%) density difference imposed by compositional differences required to achieve isopycnic conditions for the case in which the continental lithosphere is characterized by the geotherm given in Figure 15a. (c) The compositional density difference required for isopycnic conditions in Figure 15b transposed into the compositional parameter, Mg#, using equations 12a–12c and parameterizations in this study and in the work of *Jordan* [1979]. Curves L_{89} and L_{88} refer to the density-Mg# parameterization of this study for asthenospheric mantle compositions of Mg# 89 and 88 ($\alpha = 3.9 \times 10^{-5}$ °C^{-1}). Curves J_{89} and J_{88} refer to the density-Mg# parameterizations of Jordan in which $\alpha = 3.0 \times 10^{-5}$ °C^{-1}. (d) Range in Mg# for cratonic peridotites. Gray shaded region in Figure 15c shows the range of Mg# in the continental lithospheric mantle required for isopycnic conditions over the pressure range 3–6 GPa.

−0.0191 Mg# + 5.09 in the work of *Jordan* [1988]) can be used to reexpress the isopycnic condition (modified from equation (2) in the work of *Jordan* [1988]):

$$\Delta Mg\# = -\frac{\rho_0 \alpha}{(d\rho/dMg\#)} \Delta T. \qquad (12a)$$

[43] Using an average bulk thermal expansivity of α at elevated temperatures (3.9 × 10^{-5} °C^{-1} calculated by combining the thermal expansivities of each mineral at temperatures of ~1000°C using the temperature parameterizations of *Fei* [1995] at constant pressure), a $d\rho/dMg\#$ of −0.0143 (Figure 7a), and a reference asthenospheric mantle composition of Mg# 89 (ρ_0 = 3.377 g cm^{-3}), the above proportionality relationship between density and temperature for isopycnic conditions is

$$\Delta Mg\# = \Delta T/(108°C). \qquad (L_{89}) \qquad (12b)$$

This relationship is shown in Figure 15c (curve L_{89}). This is significantly different from Jordan's relationship

$$\Delta Mg\# = \Delta T/(187°C). \qquad (J_{89}) \qquad (12c)$$

of $\Delta T/(187°C)$ (curve J_{89} in Figure 15c) due to the slightly different density-Mg# relationship derived in this study and a higher thermal expansivity used by Jordan ($\alpha = 3 \times 10^{-5}$ °C^{-1}). Using an α of 3 × 10^{-5} °C^{-1} with the density-Mg# relationship of this study results in $\Delta T/(141°C)$. The effect of pressure on thermal expansivity is to lower the expansivity by ~0.85 for a pressure increase in ~4 GPa (this factor was estimated using the Anderson-Grüneisen parameter of olivine and the Birch-Murnaghan equation of state [*Fei*, 1995]). This changes equation 12b to $\Delta Mg\# = \Delta T/(124°C)$, which is bracketed by L_{89} and J_{89}.

[44] Figure 15d shows a compilation of peridotite Mg#s for various Archean cratons [*Lee et al.*, 2001]. As most cratonic mantle peridotites are derived from pressures

between 3 and 6 GPa, it can be seen from Figures 14c and 14d that cratonic peridotites are on average neutrally buoyant if the density-Mg# parameterization of this study is adopted (L_{89}). On the other hand, if Jordan's parameterization is used (J_{89}), the high Mg#s of some cratonic peridotites (Mg# $\sim$ 93) will be positively buoyant. If an asthenospheric mantle composition of Mg# $\sim$ 88 is assumed instead of Mg# $\sim$ 89, the isopcynic curves will accordingly shift to the right as shown in Figure 15c (curves L_{88} and J_{88}). Using the Mg#-density parameterization of this study, cratonic mantle would still be close to neutrally buoyant (L_{88}), but adopting Jordan's density parameterization would result in an even more extremely buoyant cratonic mantle (J_{88}).

[45] Given the uncertainty in the Mg# of the asthenospheric mantle and in the Mg#-density parameterizations, it is not possible to conclusively determine whether or not cratonic mantle is neutrally buoyant from peridotite composition data alone. However, if it is assumed that continents are essentially in isostatic equilibrium with respect to the surrounding oceanic mantle, as is implied by the lack of strong free-air gravity anomalies over continents, then certain constraints follow from the different parameterizations. If cratonic peridotites are positively buoyant, as implied by Jordan's parameterization, a missing lithology with significantly higher densities is needed to maintain a neutrally buoyant cratonic mantle. For example, using Jordan's Mg#-density parameterization (for an asthenospheric mantle with Mg# between 88 and 89), the high Mg# peridotites (93) need to be balanced by a denser lithology, such as eclogite. Assuming a minimum eclogite density of $\sim$3.52 g cm^{-3} based on a garnet/clinopyroxene ratio of $\sim$1 and garnet and clinopyroxene densities similar to peridotitic garnets and clinopyroxenes (see Table 1), the cratonic mantle at $\sim$4 GPa would consist of a minimum of 28% (by volume) of eclogite in order to maintain neutrally buoyant conditions. On the other hand, using the Mg#-density parameterization of this study, the cratonic mantle at $\sim$4 GPa could have 0–10% of this eclogite and still maintain neutral buoyancy conditions. On the basis of the revised results presented here, there is no need to call upon on large contributions of eclogitic material in the cratonic lithosphere.

7. Conclusions

[46] Densities and elastic properties of 133 natural spinel- and garnet-peridotite samples at standard temperature (25°C) and pressure (1 atm, 1 atm = 101,325 Pa) conditions (STP) were calculated for compositions ranging from Mg# ($100 \times$ Mg/(Mg + Fe)) $\sim$86−94 in order to investigate how small compositional variations in upper mantle peridotite control density and seismic velocity. The following conclusions are made:

[47] 1. V_S correlates positively with Mg# but not with olivine or orthopyroxene mode.

[48] 2. V_P does not correlate with Mg# but does exhibit a weak positive correlation with olivine mode. However, this correlation with olivine mode is likely to become even smaller at elevated pressures and temperature due to the higher-pressure derivative of orthopyroxene bulk modulus compared to olivine.

[49] 3. The ratio V_P/V_S correlates negatively with Mg# and appears to be more sensitive to variations in Mg# than in temperature.

[50] The third conclusion implies that the ratio V_P/V_S may be useful in "seeing through" the effects of temperature variation on seismic velocities as determined from seismic tomographic studies of the upper mantle. Finally, a new density versus Mg# parameterization is derived here from natural peridotites. Combined with a compilation of the Mg#s of peridotite xenoliths derived from cratonic lithospheric mantle, it can be shown that the higher Mg#s and corresponding low intrinsic densities of cratonic peridotites approximately balances the negative thermal buoyancy of cratonic lithosphere imposed by its cooler thermal state relative to upwelling asthenospheric mantle.

References

Aleksandrov, K. S., T. V. Rushova, and B. P. Belikov, The elastic properties of pyroxenes, *Sov. Phys. Crystallogr.*, 8, 589−591, 1964.

Babuska, V., J. Fiala, M. Kumazawa, I. Ohno, and Y. Sumino, Elastic properties of garnet solid-solution series, *Phys. Earth Planet. Inter.*, 16, 157−176, 1978.

Bass, J. D., Elasticity of uvarovite and andradite garnets, *J. Geophys. Res.*, 91, 7505−7516, 1986.

Bass, J. D., Elasticity of minerals, glasses, and melts, in *A Handbook of Physical Constants*, vol. 2, *Mineral Physics and Crystallography*, edited by T. J. Ahrens, pp. 45−63, AGU, Washington, DC, 1995.

Bass, J. D., and D. J. Weidner, Elasticity of single-crystal orthoferrosilite, *J. Geophys. Res.*, 89, 4359−4371, 1984.

Boyd, F. R., High- and low-temperature garnet peridotite xenoliths and their possible relation to the lithosphere-asthenosphere boundary beneath southern Africa, in *Mantle Xenoliths*, edited by P. H. Nixon, pp. 403−412, John Wiley, Hoboken, N. J., 1987.

Boyd, F. R., Compositional distinction between oceanic and cratonic lithosphere, *Earth Planet. Sci. Lett.*, 96, 15−26, 1989.

Boyd, F. R., and R. H. McAllister, Densities of fertile and sterile garnet peridotites, *Geophys. Res. Lett.*, 3, 509−512, 1976.

Boyd, F. R., and S. A. Mertzman, Composition and structure of the Kapvaal lithosphere, southern Africa, in *Magmatic Processes: Physicochemical Principles: A Volume in Honor of Hatten S. Yoder*, edited by B. O. Mysen, *Geochem. Soc. Spec. Publ.*, 1, 13−24, 1987.

Boyd, F. R., D. G. Pearson, P. H. Nixon, and S. A. Mertzman, Low-calcium garnet hazburgites from southern Africa: Their relations to craton structure and diamond crystallisation, *Contrib. Mineral. Petrol.*, 113, 352−366, 1993.

Brey, G. P., A. M. Doroshev, A. V. Girnis, and A. I. Turkin, Garnet-spinel-olivine-orthopyroxene equilibria in the FeO-MgO-Al₂O₃-SiO₂-Cr₂O₃ system, I, Composition and molar volumes of minerals, *Eur. J. Mineral.*, 11, 599−617, 1999.

Chai, M., J. M. Brown, and L. J. Slutsky, The elastic constants of an aluminous orthopyroxene to 12.5 GPa, *J. Geophys. Res.*, 102, 14,779−14,785, 1997.

Chang, Z. P., and G. R. Barsch, Pressure dependence of the elastic constants of single-crystalline magnesium oxide, *J. Geophys. Res.*, 74, 3291−3294, 1969.

Chen, C., J. A. J. Cooke, G. D. Gwanmesia, and R. C. Liebermann, Elastic wave velocities of Mg₃Al₂SiO₁₂-pyrope garnet to 10 GPa, *Am. Mineral.*, 84, 384−388, 1999.

Cynn, H., O. L. Anderson, and M. Nicol, Effects of cation disordering in a natural MgAl₂O₄ spinel observed by rectangular parallelepiped ultrasonic resonance and Raman measurements, *Pure Appl. Geophys.*, 141, 415−444, 1993.

Duffy, T. S., C. Zha, R. T. Downs, H. K. Mao, and R. J. Hemley, Elasticity of forsterite to 16 GPa and the composition of the upper mantle, *Science*, 378, 170−173, 1995.

Ehrenberg, S. N., Petrogenesis of garnet lherzolite and megacrystalline nodules from the Thumb, Navajo volcanic field, *J. Petrol.*, 23, 507−547, 1982.

Fei, Y., Thermal expansion, in *A Handbook of Physical Constants*, vol. 2, *Mineral Physics and Crystallography*, edited by T. J. Ahrens, pp. 29−44, AGU, Washington, DC, 1995.

Flesch, L. M., B. Li, and R. C. Liebermann, Sound velocities of polycrystalline MgSiO3-orthopyroxene to 10 GPa at room temperature, *Am. Mineral.*, *83*, 444–450, 1998.

Francis, D., Mantle-melt interaction recorded in spinel lherzolite xenoliths from the Alligator lake volcanic complex, Yukon, Canada, *J. Petrol.*, *28*, 569–597, 1987.

Frey, F. A., J. C. Suen, and H. W. Stockman, The Ronda high temperature peridotite: Geochemistry and petrogenesis, *Geochim. Cosmochim. Acta*, *49*, 2469–2491, 1985.

Frisillo, A. L., and G. R. Barsch, Measurement of single-crystal elastic constants of bronzite as a function of pressure and temperature, *J. Geophys. Res.*, *77*, 6360–6383, 1972.

Girnis, A. V., and G. P. Brey, Garnet-spinel-olivine-orthopyroxene equilibria in the FeO-MgO-Al2O3-SiO2-Cr2O3 system, thermodynamic analysis, *Eur. J. Mineral.*, *11*, 619–636, 1999.

Graham, E. K., Jr., and G. R. Barsch, Elastic constants of single-crystal forsterite as a function of temperature and pressure, *J. Geophys. Res.*, *74*, 5949–5960, 1969.

Graham, E. K., J. A. Schwab, S. M. Sopkin, and H. Takei, The pressure and temperature dependence of the elastic properties of single-crystal fayalite Fe2SiO4, *Phys. Chem. Miner.*, *16*, 186–198, 1988.

Griffin, W. L., S. Y. O'Reilly, and C. G. Ryan, The composition and origin of sub-continental lithospheric mantle, in *Mantle Petrology: Field Observations and High Pressure Experimentation: A Tribute to R. (Joe) Boyd*, edited by Y. Fei, C. M. Bertka, and B. O. Mysen, pp. 13–45, *Geochem. Soc. Spec. Publ.*, *6*, 1999.

Hearmon, R. F. S., The elastic constants of crystals and other anisotropic materials, in *Landolt-Börnstein TablesI/11*, edited by K. H. Hellwege and A. M. Hellwege, pp. 1–244, Springer-Verlag, New York, 1984.

Herzberg, C., Phase equilibrium constraints on the formation of cratonic mantle, in *Mantle Petrology, Field Observations and High Pressure Experimentation, A Tribute to Francis R. (Joe) Boyd*, edited by Y. Fei, C. M. Bertka, and B. O. Mysen, *Geochem. Soc. Spec. Publ.*, *6*, 241–257, 1999.

Isaak, D. G., Elastic properties of minerals and planetary objects, in *Handbook of Elastic Properties of Solids, Liquids, and Gases*, edited by M. Levy, H. E. Bass, and R. R. Stern, pp. 325–376, Academic, San Diego, Calif., 2001.

Isaak, D. G., O. L. Anderson, T. Goto, and I. Suzuki, Elasticity of single crystal forsterite measured to 1700 K, *J. Geophys. Res.*, *94*, 5895–5906, 1989.

Isaak, D. G., O. L. Anderson, and H. Oda, High-temperature thermal expansion and elasticity of calcium-rich garnets, *Phys. Chem. Miner.*, *19*, 106–120, 1992.

Isaak, D. G., E. K. Graham, J. D. Bass, and H. Wong, The elastic properties of single-crystal fayalite as determined by dynamical measurement techniques, *Pure Appl. Geophys.*, *141*, 393–414, 1993.

Jackson, J. M., S. V. Sinogeikin, and J. D. Bass, Elasticity of MgSiO3 orthoenstatite, *Am. Mineral.*, *84*, 677–680, 1999.

James, D. E., M. J. Fouch, J. C. Van Decar, and S. van der Lee, Tectospheric structure beneath southern Africa, *Geophys. Res. Lett.*, *28*, 2485–2488, 2001.

Jordan, T. H., Composition and development of the continental tectosphere, *Nature*, *274*, 544–548, 1978.

Jordan, T. H., Mineralogies, densities and seismic velocities of garnet lherzolites and their geophysical implications, in *The Mantle Sample: Inclusions in Kimberlites and Other Volcanics*, edited by F. R. Boyd and H. O. A. Meyer, pp. 1–14, AGU, Washington, DC, 1979.

Jordan, T. H., Structure and formation of the continental tectosphere, *J. Petrol.*, *1988*, 11–37, 1988.

Kandelin, J., and D. J. Weidner, Elastic properties of hedenbergite, *J. Geophys. Res.*, *93*, 1063–1072, 1988.

Kelemen, P. B., S. R. Hart, and S. Bernstein, Silica enrichment in the continental upper mantle via melt/rock reaction, *Earth Planet. Sci. Lett.*, *164*, 387–406, 1998.

Kelly, R. K., P. B. Kelemen, and M. Jull, Buoyancy of the continental upper mantle, *Geochem. Geophys. Geosys.*, *4*, doi:10.1029/2002GC000399, 2003.

Kumazawa, M., and O. L. Anderson, Elastic moduli, pressure derivatives, and temperature derivatives of single-crystal olivine and single-crystal forsterite, *J. Geophys. Res.*, *74*, 5961–5972, 1969.

Lee, C.-T., and R. L. Rudnick, Compositionally stratified cratonic lithosphere: Petrology and geochemistry of peridotite xenoliths from the Labait tuff cone, Tanzania, in *Proceedings of the VIIth International Kimberlite Conference, B. J. Dawson Volume*, edited by J. J. Gurney et al., pp. 503–521, Red Roof Design, Capetown, South Africa, 1999.

Lee, C.-T., Q. Yin, R. L. Rudnick, and S. B. Jacobsen, Preservation of ancient and fertile lithospheric mantle beneath the southwestern United States, *Nature*, *411*, 69–73, 2001.

Levien, L., D. J. Weidner, and C. T. Prewitt, Elasticity of diopside, *Phys. Chem. Miner.*, *4*, 105–113, 1979.

Lewis, M. F., Elastic constants of magnesium aluminate spinel, *J. Acoust. Soc. Am.*, *40*, 728–729, 1966.

Li, B., G. D. Gwanmesia, and R. C. Liebermann, Sound velocities of olivine and beta polymorphs of Mg2SiO4 at Earth's transition zone pressures, *Geophys. Res. Lett.*, *23*, 2259–2262, 1996.

Li, B., C. Chen, G. D. Gwanmesia, and R. C. Liebermann, Sound velocity measurements at mantle transition zone conditions of pressure and temperature using ultrasonic interferometry in multianvil apparatus, in *Properties of Earth and Planetary Materials at High Pressure and Temperature*, *Geophys. Monogr. Ser.*, vol. 101, edited by M. H. Manghnani and T. Yagi, pp. 41–61, AGU, Washington, DC, 1998.

Liu, H.-P., R. N. Schock, and D. L. Anderson, Temperature dependence of single-crystal spinel (MgAl2O4) elastic constants from 293 to 423°K measured by light-sound scattering in the Raman-Nath region, *Geophys. J. R. Astron. Soc.*, *42*, 217–250, 1975.

McDonough, W. F., Constraints on the composition of the continental lithospheric mantle, *Earth Planet. Sci. Lett.*, *101*, 1–18, 1990.

McDonough, W. F., and F. A. Frey, Rare earth elements of upper mantle rocks, in *Geochemistry and Mineralogy of Rare Earth Elements*, edited by B. R. Lipin and G. McKay, *Rev. Mineral.*, *21*, 99–145, 1989.

McDonough, W. F., and S.-S. Sun, The composition of the Earth, *Chem. Geol.*, *120*, 223–253, 1995.

Menzies, M. A., Cratonic, circumcratonic and oceanic mantle domains beneath the western U.S.A., *J. Geophys. Res.*, *94*, 7899–7915, 1989.

Menzies, M. A., C. Dupuy, and A. Nicolas, Orogenic lherzolite and mantle processes, in *Special Volume*, edited by the *Journal of Petrology*, 310 pp., Oxford Univ. Press, New York, 1991.

Nixon, P. H., N. W. Rogers, I. L. Gibson, and A. Grey, Depleted and fertile mantle xenoliths from southern African kimberlites, *Annu. Rev. Earth Planet. Sci.*, *9*, 285–309, 1981.

Olijnyk, H., E. Paris, C. A. Geiger, and G. A. Lager, Compressional study of katoite [Ca3Al2(O4H4)3] and grossular garnet, *J. Geophys. Res.*, *96*, 14,313–14,318, 1991.

O'Neill, H. S. C., The transition between spinel lherzolite and garnet lherzolite, and its use as a geobarometer, *Contrib. Mineral. Petrol.*, *77*, 185–194, 1981.

Poudjom, D., H. Yvette, S. Y. O'Reilly, W. L. Griffin, and P. Morgan, The density structure of subcontinental lithosphere through time, *Earth Planet. Sci. Lett.*, *184*, 605–621, 2001.

Rudnick, R. L., W. F. McDonough, and B. W. Chappell, Carbonatite metasomatism in the northern Tanzanian mantle: Petrographic and geochemical characteristics, *Earth Planet. Sci. Lett.*, *114*, 463–475, 1993.

Rudnick, R. L., W. F. McDonough, and A. Orpin, Northern Tanzanian peridotite xenoliths: A comparison with Kaapvaal peridotites and inferences of metasomatic reactions, in *Kimberlites, Related Rocks and Mantle Xenoliths*, edited by H. O. A. Meyer and O. H. Leonardos, *CPRM Spec. Publ.,1A*, 336–353, 1994.

Sato, Y., M. Akaogi, and S.-I. Akimoto, Hydrostatic compression of the synthetic garnets pyrope and almandine, *J. Geophys. Res.*, *83*, 335–338, 1978.

Shi, L., D. Francis, J. Ludden, A. Frederiksen, and M. Bostock, Xenolith evidence for lithospheric melting above anomalously hot mantle under the northern Canadian Cordillera, *Contrib. Mineral. Petrol.*, *131*, 39–53, 1998.

Shirey, S. B., J. W. Harris, S. R. Richardson, M. J. Fouch, D. E. James, P. Cartigny, P. Deines, and F. Viljoen, Diamond genesis, seismic structure, and evolution of the Kaapvaal-Zimbabwe craton, *Science*, *297*, 1683–1686, 2002.

Sumino, Y., The elastic constants of Mn2SiO4, Fe2SiO4, and Co2SiO4, and the elastic properties of olivine group minerals at high temperature, *J. Phys. Earth*, *27*, 209–238, 1979.

Sumino, Y., O. Nishizawa, T. Goto, I. Ohno, and M. Ozima, Temperature variation of elastic constant of single-crystal forsterite between −190 and 400°C, *J. Phys. Earth*, *25*, 377–392, 1977.

Suzuki, I., O. L. Anderson, and Y. Sumino, Elastic properties of a single-crystal forsterite Mg2SiO4 up to 1,200 K, *Phys. Chem. Miner.*, *10*, 38–46, 1983.

Suzuki, I., I. Ohno, and O. L. Anderson, Harmonic and anharmonic properties of spinel MgAl2O4, *Am. Mineral.*, *85*, 304–311, 2000.

Takahashi, T., and L.-G. Liu, Compression of ferromagnesian garnets and the effect of solid solutions on the bulk modulus, *J. Geophys. Res.*, *75*, 5757–5766, 1970.

Wang, H., and G. Simmons, Elasticity of some mantle crystal structures: 1. Pleonaste and hercynite spinel, *J. Geophys. Res.*, *77*, 4379–4392, 1972.

Watt, J. P., G. F. Davies, and R. J. O'Connell, The elastic properties of composite materials, *Rev. Geophys.*, *14*, 541–563, 1976.

Weaver, J. S., T. Takahashi, and J. Bass, Isothermal compression of grossular garnets to 250 kbar and the effect of calcium on the bulk modulus, *J. Geophys. Res.*, *81*, 2475–2482, 1976.

Webb, S., and I. Jackson, The pressure dependence of the elastic moduli of single-crystal orthopyroxene $(Mg_{0.8}Fe_{0.2})SiO_3$, *Eur. J. Mineral.*, *5*, 1111–1119, 1993.

Weidner, D. J., H. Wang, and J. Ito, Elasticity of orthoenstatite, *Phys. Earth Planet. Inter.*, *17*, P7–P13, 1978.

Wilshire, H. G., C. E. Meyer, J. K. Nakata, L. C. Calk, J. W. Shervais, J. E. Nielson, and E. C. Schwarzman, Mafic and ultramafic xenoliths from volcanic rocks of the western United States, *U.S. Geol. Surv. Pap., 1443*, 179 pp., 1988.

Wilshire, H. G., A. V. McGuire, J. S. Noller, and B. D. Turrin, Petrology of lower crustal and upper mantle xenoliths from the Cima volcanic field, California, *J. Petrol.*, *32*, 169–200, 1991.

Yoneda, A., Pressure derivatives of elastic constants of single crystal MgO and $MgAl_2O_4$, *J. Phys. Earth*, *38*, 19–55, 1990.

Yoneda, A., and M. Morioka, Pressure derivatives of elastic constants of single-crystal forsterite, in *High Pressure Research: Applications to Earth and Planetary Sciences*, edited by Y. Syono and M. H. Manghnani, pp. 207–214, AGU, Washington, DC, 1992.

Zhang, L., H. Ahsbahs, and A. Kutoglu, Hydrostatic compression and crystal structure of pyrope to 33 GPa, *Phys. Chem. Miner.*, *25*, 301–307, 1998.

Zhang, L., H. Ahsbahs, A. Kutoglu, and C. A. Geiger, Single-crystal hydrostatic compression of synthetic pyrope, almandine, spessartine, grossular and andradite garnets at high pressures, *Phys. Chem. Miner.*, *27*, 52–58, 1999.

_____

C.-T. A. Lee, Department of Earth Science, Rice University, MS 126, P.O. Box 1892, Houston, TX 77251, USA. (ctlee@rice.edu)